

## A case study of convective organization into precipitating lines in the Southwest Amazon during the WETAMC and TRMM-LBA

M. A. F. Silva Dias,<sup>1</sup> W. Petersen,<sup>2</sup> P. L. Silva Dias,<sup>1</sup> R. Cifelli,<sup>2</sup> A. K. Betts,<sup>3</sup>  
M. Longo,<sup>1</sup> A. M. Gomes,<sup>4</sup> G. F. Fisch,<sup>5</sup> M. A. Lima,<sup>4</sup> M. A. Antonio,<sup>4</sup>  
and R. I. Albrecht<sup>1</sup>

Received 16 January 2001; revised 3 October 2001; accepted 9 October 2001; published 27 September 2002.

[1] A case study of convective development in the Southwest Amazon region during the Wet Season Atmospheric Mesoscale Campaign (WETAMC) and Tropical Rainfall Measuring Mission (TRMM)/Large-Scale Biosphere-Atmosphere (LBA) Experiment in Amazonia is presented. The convective development during 7 February 1999 is shown to occur during a period of very weak large-scale forcing in the presence of topography and deforestation. The available data include dual Doppler radar analysis, radiosonde launches, and surface and boundary layer observations. The observational analysis is complemented with a series of model simulations using the RAMS with 2-km resolution over a 300 km × 300 km area forced by a morning radiosonde profile. A comparison of the observed and simulated thermodynamic transformation of the boundary layer and of the formation of convective lines, and of their kinematic and microphysical properties is presented. It is shown that only a few very deep and intense convective cells are necessary to explain the overall precipitating line formation and that discrete propagation and coupling with upper atmosphere circulations may explain the appearance of several lines. The numerical simulation indicates that topography may be the cause of initial convective development, although later on the convective line is parallel to the midlevel shear. There are indications that small-scale deforestation may have an effect on increasing rainfall in the wet season when the large-scale forcing is very weak. *INDEX TERMS*: 0315 Atmospheric Composition and Structure: Biosphere/atmosphere interactions; 3307 Meteorology and Atmospheric Dynamics: Boundary layer processes; 3314 Meteorology and Atmospheric Dynamics: Convective processes; 3322 Meteorology and Atmospheric Dynamics: Land/atmosphere interactions

**Citation:** Silva Dias, M. A. F., et al., A case study of convective organization into precipitating lines in the Southwest Amazon during the WETAMC and TRMM-LBA, *J. Geophys. Res.*, 107(D20), 8078, doi:10.1029/2001JD000375, 2002.

### 1. Introduction

[2] A major goal of the Large-Scale Biosphere-Atmosphere (LBA) Experiment in Amazônia is to better understand the coupling between atmospheric convection and land surface variability and its impact on the hydrologic cycle in Amazônia. During the Wet Season Atmospheric Mesoscale Campaign (WETAMC)/LBA and Tropical Rainfall Measuring Mission (TRMM)/LBA, several convective

lines occurred with different degrees of organization [Cifelli *et al.*, 2002; Machado *et al.*, 2002; Pereira Filho *et al.*, 2002; Carvalho and Jones, 2001]. Most of the cases were observed to propagate over the WETAMC and TRMM network of observing platforms as mature systems or as systems formed by the outflow interactions of previous convection formed elsewhere. On 7 February 1999 there was a unique opportunity to observe the complete evolution of a squall line beginning with the formation of scattered clouds in the early morning and concluding with the development of an organized line of deep convective cells. Importantly, the organization of the squall line occurred well within the dual-Doppler coverage area of the S-POL and TOGA radars (see Cifelli *et al.* [2002] and Silva Dias *et al.* [2002] for locations of the radars).

[3] Greco *et al.* [1990] classified convective systems forming in the Amazon region as Coastal Occurring Systems (COS), Basin Occurring Systems (BOS) and Locally Occurring Systems (LOS). A significant fraction of the convection classified as COS represented very large squall

<sup>1</sup>Department of Atmospheric Science, University of São Paulo (USP), São Paulo, Brazil.

<sup>2</sup>Department of Atmospheric Science, Colorado State University (CSU), Fort Collins, Colorado, USA.

<sup>3</sup>Atmospheric Research, Pittsford, Vermont, USA.

<sup>4</sup>Institute of Meteorological Research, State University of São Paulo (UNESP), São Paulo, Brazil.

<sup>5</sup>Institute of Space Activities, Aeronautics Technological Center (CTA), USA.

lines that have been studied by *Silva Dias and Ferreira* [1992] and by *Cohen et al.* [1995]. These squall lines and their associated mesoscale boundaries are formed at the northern coast of South America, are triggered by the sea breeze circulation, and can propagate well into the interior of the Amazon basin as organized entities for up to several days. *Garstang et al.* [1994] and *Greco et al.* [1994] studied the kinematic and diabatic heat and moisture transports of several COS that were observed during ABLE 2B [*Harriss et al.*, 1990] using a radiosonde and surface mesonet network in near Manaus.

[4] BOS are convective lines that form in the basin and also show propagation but with lifetimes of a few hours. LOS are smaller, short-lived, more isolated convective systems that tend to peak in phase with diurnal heating. In the definition of *Orlanski* [1975], COS, BOS, and LOS would be classified as meso- $\alpha$ , meso- $\beta$  and meso- $\gamma$  systems, respectively.

[5] During the WETAMC, at least one case of COS with a very long lifetime was observed and this case is described by *Betts et al.* [2002a]. *Cifelli et al.* [2002] contrasted the vertical structure of two convective systems occurring in different low-level wind regimes (i.e., easterly versus westerly) during WETAMC and TRMM-LBA. The “westerly” event was a BOS while the classification of the “easterly” case was ambiguous and may have been either BOS or COS. *Cifelli et al.* found significant differences in the kinematic and microphysical characteristics of the two systems. The convective system observed in Rondônia during the afternoon of 7 February 1999 can be classified as BOS. Unlike convection described in the previous studies discussed above, the 7 February system appeared to develop independently of obvious influences from previous convection or other large-scale boundary interactions.

[6] This paper will build upon observations made during the WETAMC and TRMM/LBA by several observing platforms, and by high resolution numerical simulations performed with the Regional Atmospheric Modeling System (RAMS) [*Pielke et al.*, 1992] to describe and discuss the organization of the 7 February 1999 convection. Section 2 describes both the data and methodology used in this study. Section 3 presents the observed large-scale surface and boundary layer evolution from the early morning through afternoon hours and section 4 discusses kinematic and microphysical aspects of storm evolution as observed by the S-POL and TOGA radars. Results from the numerical simulation are presented in section 5 including a discussion of the impact of topography and surface vegetation cover in the observed development. Last, section 6 summarizes the observations and presents the conclusions.

## 2. Data, Methodology, and Model

[7] Radar data from the NCAR S-POL (S-band, dual-polarized) and NASA TOGA radar (C-band, linear-polarized) were utilized to retrieve the three-dimensional wind field and to examine cloud microphysical properties for the 7 February event. A description of the radar locations, scanning strategies, and parameters collected by the radars are given by *Cifelli et al.* [2002].

[8] A total of 15 volumes of S-POL and TOGA radar data were analyzed for the time period 1530–1810 UTC.

These data allowed for the mesoscale structure of convection to be examined at 10 min resolution with the exception of two time periods in which dual-Doppler could not be performed due to missing scans from the TOGA radar (1720 and 1800 UTC). The dual-Doppler analysis procedure involved manually unfolding the radial velocity data, interpolating to a 103 km  $\times$  103 km  $\times$  16.5 km Cartesian grid (1  $\times$  1  $\times$  0.5 km spacing) and combining the data to retrieve the three dimensional wind field. Prior to unfolding, the S-POL data were processed to eliminate ground clutter and calculate specific differential phase (KDP) from total differential phase ( $\Psi$ DP) data as described by *Carey et al.* [2000]. A complete description of the radar analysis procedure is given by *Cifelli et al.* [2002].

[9] Surface data from weather stations at Rebio Jaru and Rolim de Moura [*Silva Dias et al.*, 2002, see Figure 2 for locations] were obtained with 30 min resolution while the data from the pasture site at Fazenda Nossa Senhora, also known as the Anglo-Brazilian Amazonian Climate Observation Study (ABRACOS) [*Gash et al.*, 1996] site, was obtained at 5 min resolution [see *Fuentes et al.*, 2000]. The ABRACOS site is located in a pasture area at approximately 2 km from the TOGA radar. The surface data [cf. *Betts et al.*, 2002b, for the instrumentation at this site] have been screened for tendencies and compared with radiosonde first level data off the surface. For the purpose of this case study, suspicious data have been removed and left as missing data. The radiosonde data has undergone a full quality control procedure. The stations of Rebio Jaru and Rolim de Moura operated Vaisala equipment while ABRACOS and Rancho Grande operated VIZ equipment.

[10] The Rolim de Moura sounding of 1200 UTC (Local time is UTC minus 4 hours) located at 11°42'17"S and 61°46'38"W was used for a horizontally homogeneous initialization of RAMS. Tests were performed also with the 1200 UTC ABRACOS sounding but due to a very humid layer below 1 km, an unrealistic stratus deck formed in the simulation, hindering surface solar heating and further development of the mixed layer. One single grid has been used in the model simulations with 2-km resolution centered close to the city of Ji-Paraná at 10.87°S, 61.83°W. A stretched vertical grid has been used, starting at 150 m resolution just above the surface and stretching gradually by a factor of 1.2 in successive layers until reaching a maximum spacing of 1 km, and then kept constant up to model top which is set at approximately 25 km. The first level for wind, temperature, and mixing ratios is 71 m above ground level (AGL). The simulated grid matrix has 151  $\times$  149  $\times$  31 points. Surface files describing topography, vegetation and percent of land versus water in a grid cell have been obtained from an IGBP (International Geosphere Biosphere Program) 1-km resolution data set. The full microphysics suite of RAMS version 4.3 has been used in all simulations [*Walko et al.*, 1995] with pristine ice having prognostic concentration while the other ice have specified mean diameter. Cumulus parameterization has been turned off since clouds are supposedly being resolved with this model resolution. Initial values of soil moisture, constant over the whole domain at the initial time, have been used to tune the surface fluxes to the observations as will be discussed in

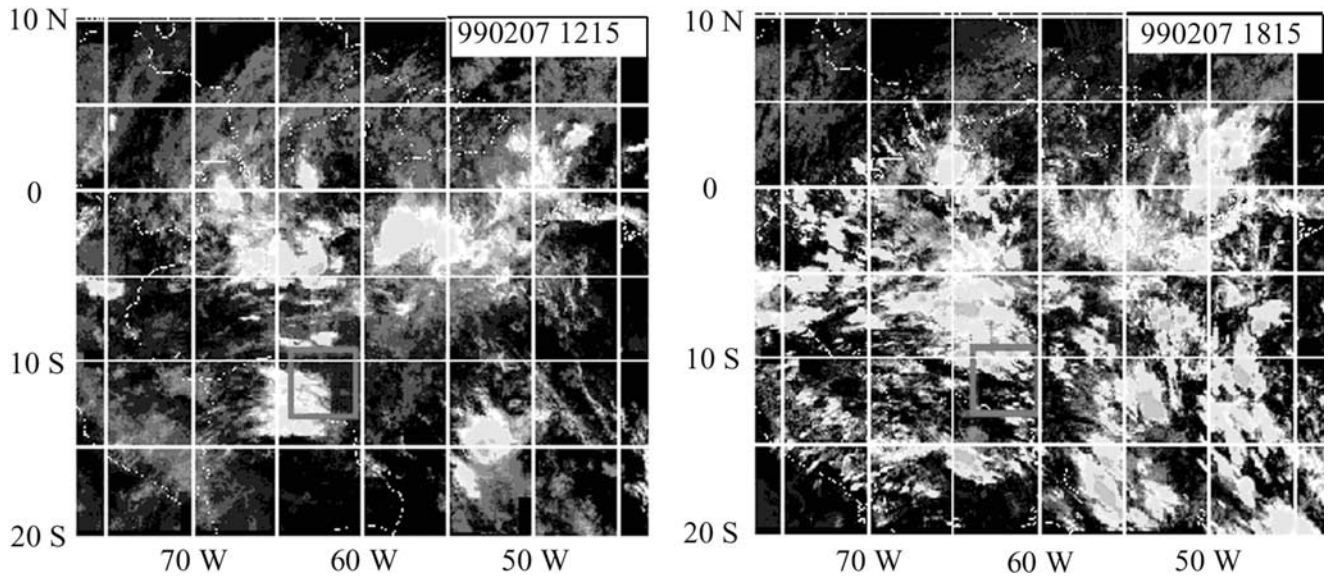


**Figure 1.** Infrared GOES satellite images. The red square is the study area in Rondônia. (a) 7 Feb. 1999, 1215 UTC; (b) 7 Feb. 1999, 1815 UTC. Colors are associated to threshold IR temperatures: yellow for  $230\text{K} < T_{\text{ir}} < 210\text{K}$ ; green for  $210\text{K} < T_{\text{ir}} < 190\text{K}$ .

section 5. The model run with all the above mentioned options is referred to as the control run.

### 3. Large-Scale, Surface, and Boundary Layer Evolution

[11] Figure 1 shows the infrared satellite images for 7 February 1999 at 1215 and 1815 UTC. The red square

indicates the study area in the SW Amazon over the Brazilian state of Rondônia. A previous day Mesoscale Convective System (MCS) located in SW Rondônia decayed in the early morning hours. At 1215 UTC the NE half of the study region has clear skies. By 1815 UTC Figure 1b shows the NW/SE oriented line that will be discussed in the following sections.

[12] The large-scale situation over SW Amazon Basin, specifically over the state of Rondônia, in the early morning

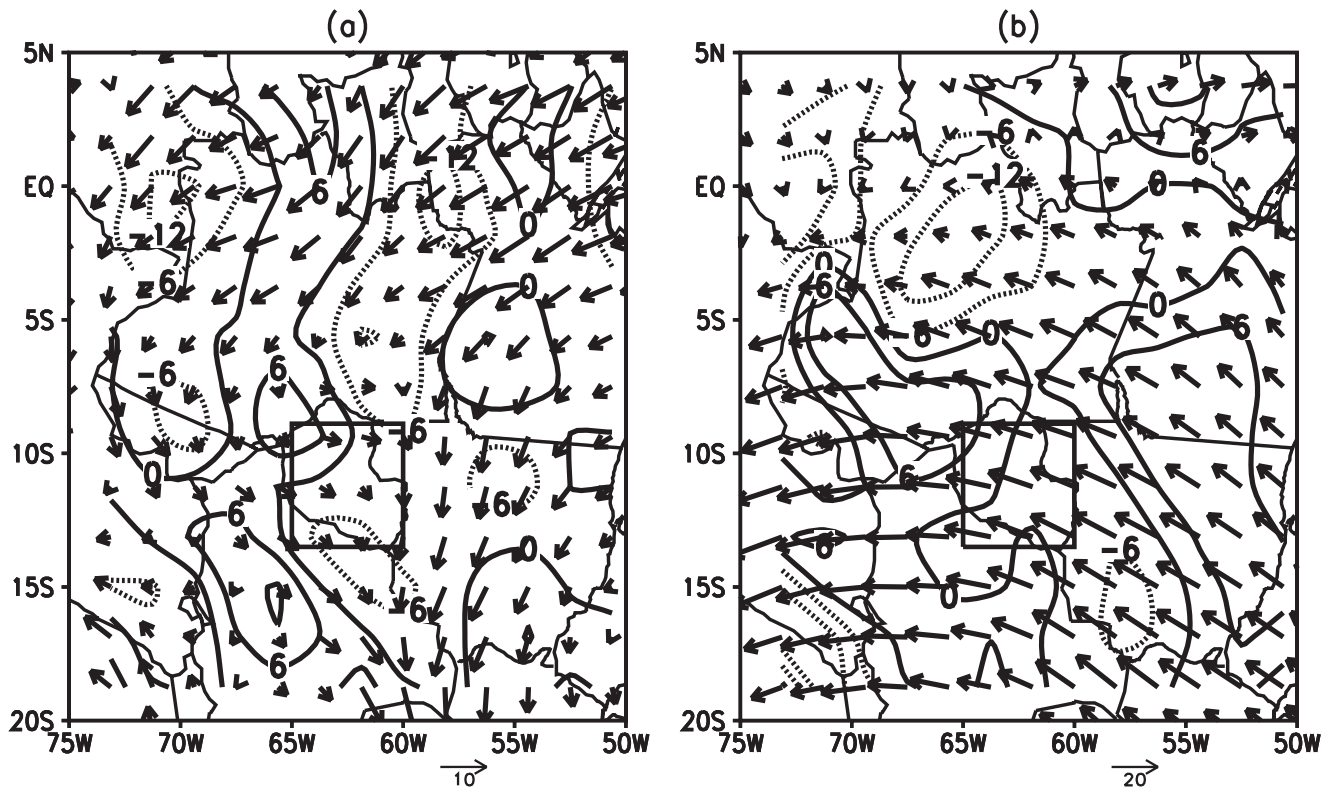


**Figure 2.** Winds from the global CPTEC analysis for 7 Feb. 1999, 1200 UTC and divergence (labels in  $10^{-6} \text{ s}^{-1}$ ). (a) 925 hPa; (b) 100 hPa. The square is around the study area, the state of Rondônia.

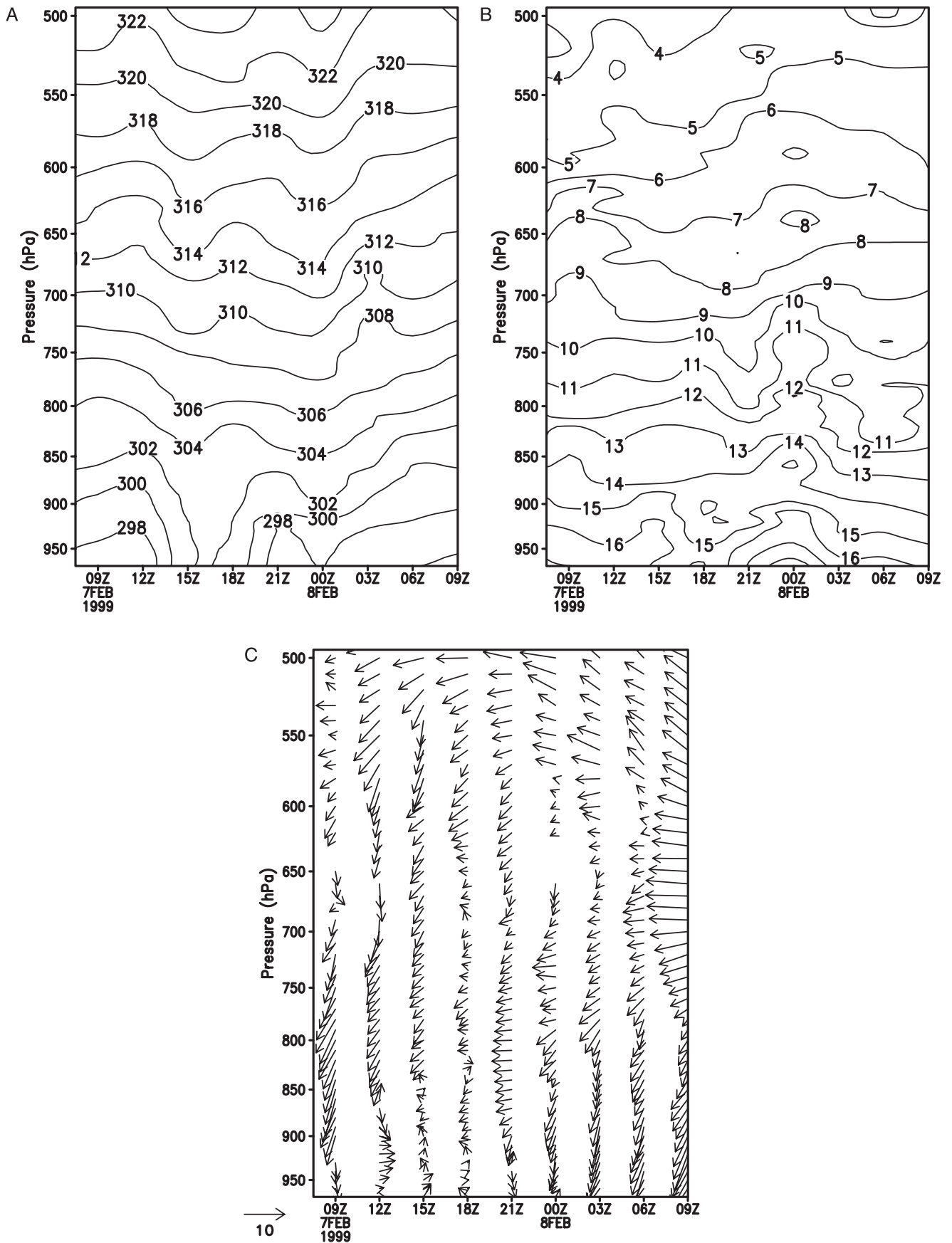


**Figure 3.** Temporal evolution of the vertical profile of potential temperature (a) and specific humidity (b) and wind (shaded areas show wind speed greater than 4 m s<sup>-1</sup>) (c) from the ABRACOS site radiosonde launch.

**Table 1.** Time Evolution of the Height of CBL Over the Pasture Site (ABRACOS)<sup>a</sup>

	12 UTC	15 UTC	18 UTC	21 UTC
7 Feb. 1999	90	600	850	???
8 Feb. 1999	50	400	850	
Average (from Fisch et al., submitted manuscript, 2001)	94	475	765	927

<sup>a</sup>Heights are in meters.

of 7 February 1999 indicated very weak forcing from the large scale (about  $\pm 0.4 \text{ cm s}^{-1}$  at 850 hPa). The winds at the low level shown in Figure 2a were from the NW responding to the remains of a mid latitude frontal system approaching from Southern Brazil, Paraguay and Southern Bolivia (T. M. Rickenbach et al., Modulation of convection in the western Amazon basin by extratropical baroclinical waves, submitted to *Journal of Geophysical Research*, 2001, hereinafter referred to as Rickenbach et al., submitted manuscript, 2001). Actually, 7 February was an interesting day from a regime perspective, as it actually was a day of transition from westerly to easterly regimes according to Rickenbach et al. (submitted manuscript, 2001) definition: the soundings from ABRACOS in Figure 3c show low level winds were starting to turn by 1500 UTC. Low level convergence was found west of the study area in the central part of the Amazon Basin collocated with upper level divergence as may be seen in Figure 2b. Rondônia was at the eastern edge of this pattern close to the no divergence line.

[13] The interest in this case lies in the fact that no significant large-scale forcing was evident. Convection ini-

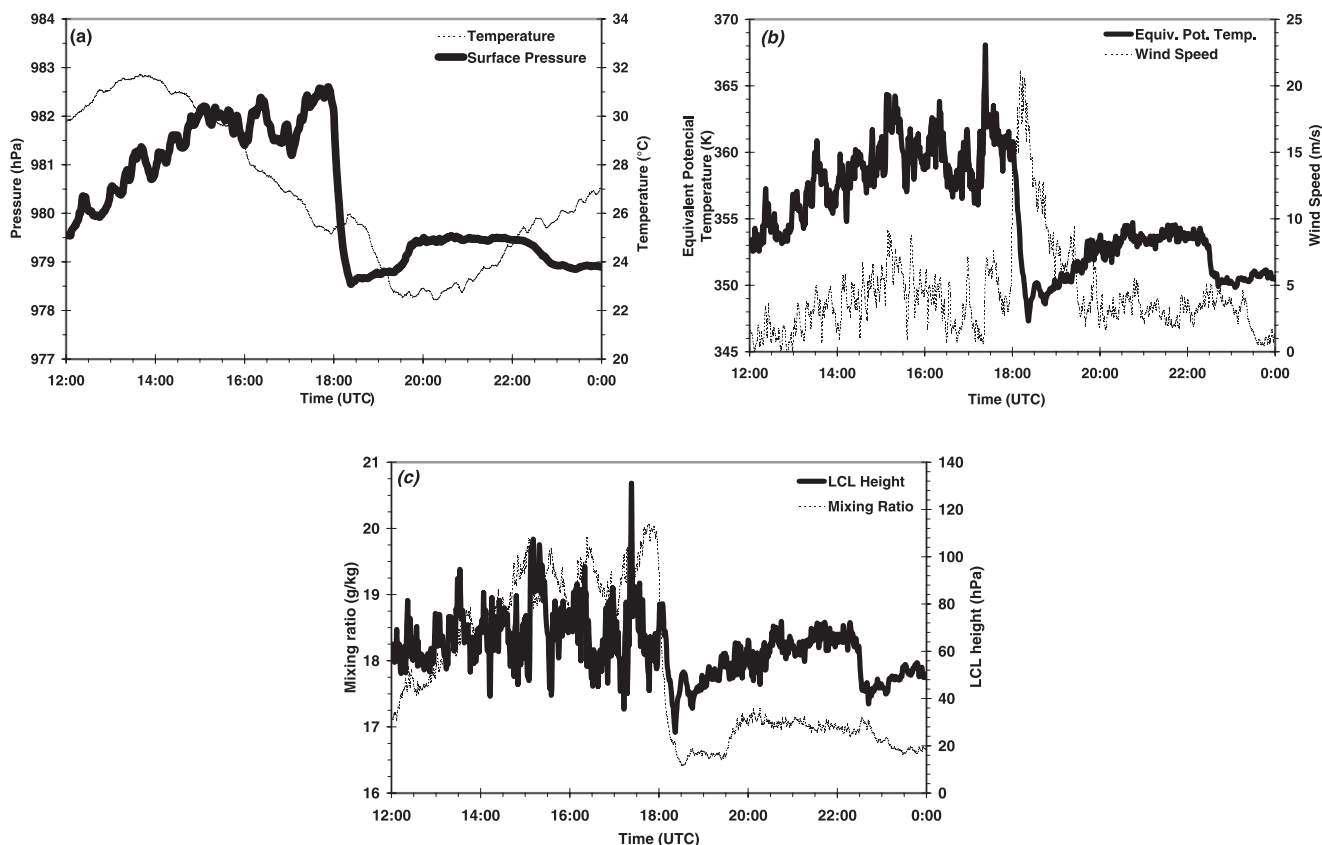
**Table 2.** Some Thermodynamics Variables for 7 February 1999 From the ABRACOS Soundings

	12 UTC	15 UTC	18 UTC	21 UTC
Surface Thetae, K	348.4	352.8	352.0	348.4
CAPE, $\text{J kg}^{-1}$	1155	1365	1299	5
LCL, hPa	963.1	884.4	882.4	951.1
CIN, $\text{J kg}^{-1}$	53.1	84.4	32.4	11.1
Surface q, $\text{g kg}^{-1}$	17.0	16.2	15.9	16.7

tiated in apparent randomness in response to diurnal heating. The convection started during the morning as small convective cells; a few systems grew and got organized into several convective bands that were about 300–400 km long, travelling at low speeds and with a lifetime of several hours.

[14] The first thunderstorms reached the ABRACOS site by 18 UTC (14:00 LT) affecting the growth of the boundary layer. Table 1 shows the time evolution of the height of the convective boundary layer (CBL) for 7 February 1999. Development of the CBL depth was remarkable, extending to a depth of 85 m higher than the average for the whole WETAMC. Figure 3 shows a sequence of soundings at the ABRACOS site: the sounding of 1800 UTC was launched just prior to the arrival of the first gust-front. By 2100 UTC, it was impossible to characterize the height of the CBL, as the whole boundary layer became very stable and was overlaid by stratiform clouds. At 12 UTC, the convective available potential energy (CAPE) had a value of  $1155 \text{ J kg}^{-1}$  (see Table 2). At 18 UTC, prior to the arrival of the gust front CAPE increased to  $1365 \text{ J kg}^{-1}$ .

[15] Figure 4 shows the detailed evolution of some surface thermodynamic variables, temperature and pressure on

**Figure 4.** Time series of surface thermodynamic variables at the ABRACOS pasture site on 7 Feb. 1999.

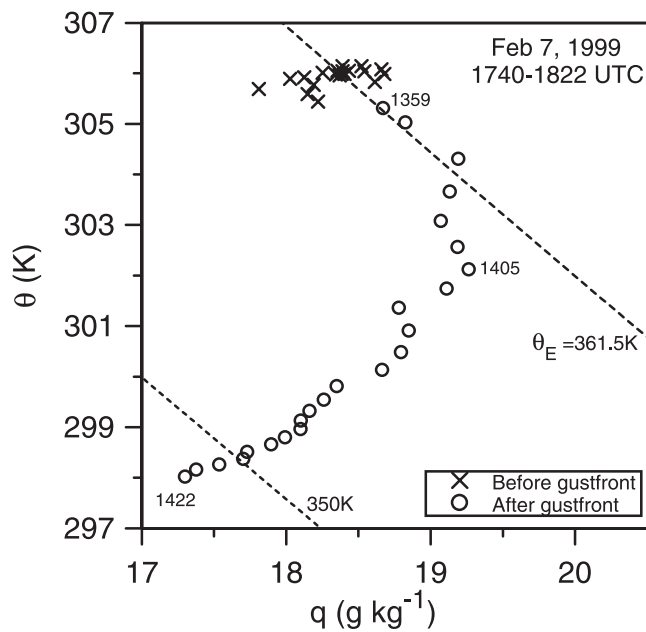


**Figure 5.**  $(q, \theta)$  plot, showing the arrival of the gust-front at 1359 LST.

the upper panel, equivalent potential temperature,  $\theta_E$ , and surface wind speed, on the middle panel, and water vapor mixing ratio  $q$ , and pressure height from surface to the lifting condensation level (LCL),  $\Delta p_{NCL}$ , calculated from measurements at 1.5 m height. From 1200 to 1500 UTC, temperature,  $\Delta p_{LCL}$  and  $\theta_E$  all rise to reach roughly their maximum values for the day, while mixing ratio fluctuates around  $18.5 \text{ g.kg}^{-1}$ . During this period,  $q$  is kept from rising, despite the large surface evaporation, by the upward transport of moisture into shallow cumulus clouds. About 1500 UTC the convective clouds start to organize first into

bands of congestus (cf. Figure 9) and the fluctuations of  $T$ ,  $p_{LCL}$  and  $\theta_E$  get larger as the site is influenced by showers. The passage of the line at 1800 UTC is very distinct, and is marked by large falls in these same three variables as the surface gust-front reaches the site at 1759 UTC, with maximum wind speed greater than  $20 \text{ m s}^{-1}$ . The outflow air produces a temperature drop of about 7K and a drop in  $\theta_E$  of 13K in about 20 min, and is nearly saturated (relative humidity about 90%, and  $\Delta p_{LCL}$  falls from 110 to less than 20 hPa in about 30 min).

[16] The outflow air however is barely drier in mixing ratio suggesting that the boundary layer is affected by separate evaporative and downdraft transport processes. Figure 5 shows the data just before and after the arrival of the gust-front on a  $(q, \theta)$  plot. The cluster of points marked with an x shows the 1 min surface fluctuations for a period of 20 min ahead of the gust front. The data after the arrival of the gust-front (circles) at 1759 UTC are also 1 min apart and some are labeled with their time. Initially,  $\theta$  falls and  $q$  rises at constant  $\theta_E = 361.5\text{K}$  (dotted line shown), corresponding to a mean of the value ahead of the gust-front. This indicates high  $\theta_E$  air modified just by the evaporation of rain. However, around 1805 UTC the trajectory changes sharply on the figure, as  $\theta$  and  $q$  both fall steeply (and along with them,  $\theta_E$  to below 350K). This change of trajectory indicates the arrival of cooler, drier downdraft air from above.

[17] The transition in the structure of outflow air has been noticed in earlier studies [e.g., *Betts*, 1984], and recently *Tompkins* [2001], from a numerical simulation, has drawn attention to the fact that the triggering of new convection by cold pool outflows over the ocean appears to involve the lifting of this cooled but high  $\theta_E$  air, although over the ocean, the surface heat flux rapidly restores the temperature.

[18] The tethersonde profiles at the ABRACOS site show the BL structure before and after the passage of the convective band. Figures 6a and 6b show the sequence

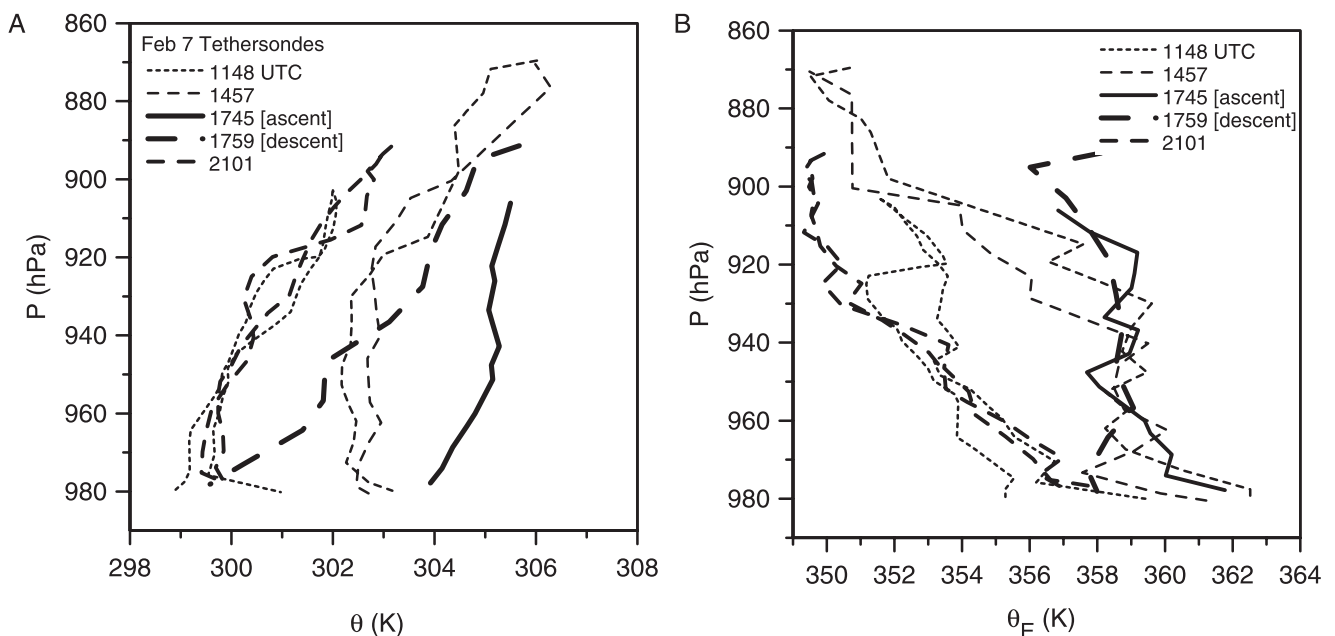


**Figure 6.** Sequence of tethersonde BL profiles of  $\theta$  and  $\theta_E$  at ABRACOS site on 7 February.

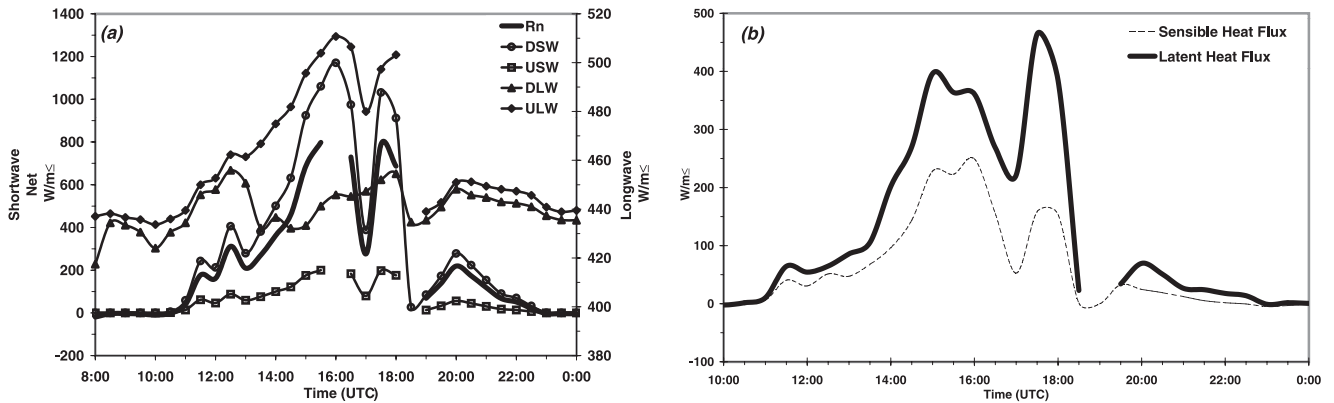


**Figure 7.** (a) Downward and upward shortwave (left axis) and longwave (right axis) irradiance and net irradiance (left axis). (b) Sensible and Latent heat fluxes; at ABRACOS site on 7 February.

of BL profiles of  $\theta$  and  $\theta_E$  with mean times at 1148, 1457, 1752 and 1901 UTC. For each there is an ascent and descent profile, but we have only distinguished them for the ascent and descent pair just before 1800 UTC, because this descent profile was just at the arrival time of the first gust-front. Considering the sequence from 1148 to 1745 UTC, we see the warming and deepening of the nearly mixed boundary layer (BL), and an increase in BL  $\theta_E$  from values of order 354K to 359K. At 1500 UTC, the mixed layer (ML) depth is about 70 hPa, consistent with  $p_{LCL}$  in Figure 4. The 1745 UTC ascent profile is just showing signs of cooling near the surface. About 15 min later, the 1759 UTC descent profile (heavy dashes) is just at the time of arrival of the gust-front and it shows a large cooling, but  $\theta_E$  has barely started to fall as the tether sonde is drawn down to the surface, because this is just ahead of the arrival of the low  $\theta_E$  downdraft air, as discussed above. By the time of the following profile, near 2101 UTC, the passage of the convective line has transformed the BL back to a cooler, more stable structure, with a lower  $\theta_E$  very similar to that in the morning. In fact, the morning structure was itself established by convection during the previous night.

[19] Figure 7a shows all radiation components measured at the ABRACOS site. Downward shortwave irradiance (DSW) representing solar incoming radiation has a strong diurnal cycle. After sunrise (1100 UTC), the absolute value of DSW starts to rise, with some variability due to some cloud cover. After a maximum absolute value ( $1170 \text{ W m}^{-2}$ ) at about 1600 UTC, DSW falls to  $388 \text{ W m}^{-2}$  at 1700 UTC due to cloudiness. DSW recovered higher values at 1730 UTC ( $1032 \text{ W m}^{-2}$ ) although it drops to  $27 \text{ W m}^{-2}$  after the convective line passage (1830 UTC), leading the net radiation to  $-58 \text{ W m}^{-2}$ . Upward shortwave irradiance (USW) shows similar features but with smaller values. Upward longwave irradiance (ULW) represents irradiance emitted by the surface and is seen to increase by sunrise, reaching a maximum value at 1600 UTC -  $511 \text{ W m}^{-2}$ . A slight ULW decrease is observed at 1700 UTC, emphasizing the passage of some convective cells, followed by an increase. At 1800 UTC ULW was  $503 \text{ W m}^{-2}$  and it fell to  $439 \text{ W m}^{-2}$  at 1900 UTC, due to the cooling effect of the downdrafts. Afterwards, ULW did not recover the original values, remaining at  $450 \text{ W m}^{-2}$ .

[20] Figure 7b shows sensible and latent heat fluxes (SH and LH, respectively). Both start to increase after sunrise, reaching maximum values at 1500 UTC (LH) and 1600 UTC (SH), with a Bowen ratio of about 0.6 when there is a rapid fall followed by an increase. At 1830 UTC, both SH and LH drop to zero and do not return to high values. Figure 8 shows the number of raingages (from a total of 40 in the area) that observed 5 min rainfall rates over different thresholds ( $20, 40, 60$  and  $80 \text{ mm.hr}^{-1}$ ) during the afternoon. It shows that high rainfall rates occurred between 1700 and 1830 UTC and a few sites observed rainfall rates over  $60$  and  $80 \text{ mm.hr}^{-1}$ .

#### 4. Radar Observations of Storm Evolution

[21] Low-level radar CAPPI's of reflectivity and horizontal wind flow were used to determine the overall trend in convective organization during the 1530–1810 UTC analysis period. For the dual-Doppler analysis, an average storm motion vector was calculated for each radar volume in order to perform a differential advection in the combined dual-Doppler synthesis. Inspection of successive low-level CAPPI (Constant Altitude Plan Position Indicator) plots showed that the average storm motion direction remained nearly constant throughout the analysis period (motion from

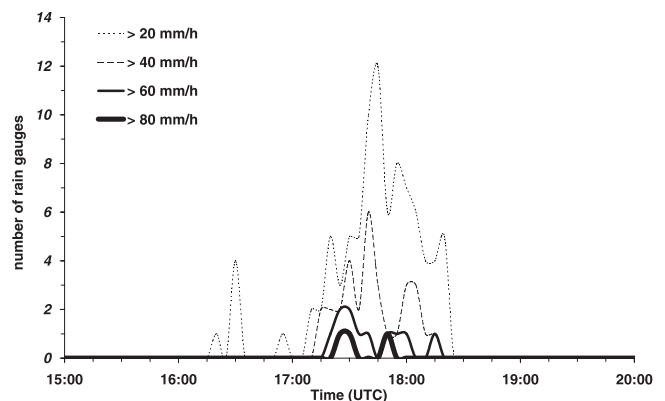


**Figure 8.** Number of raingages in all networks (42 raingages) that measured 5 min rainfall rates above the given thresholds.

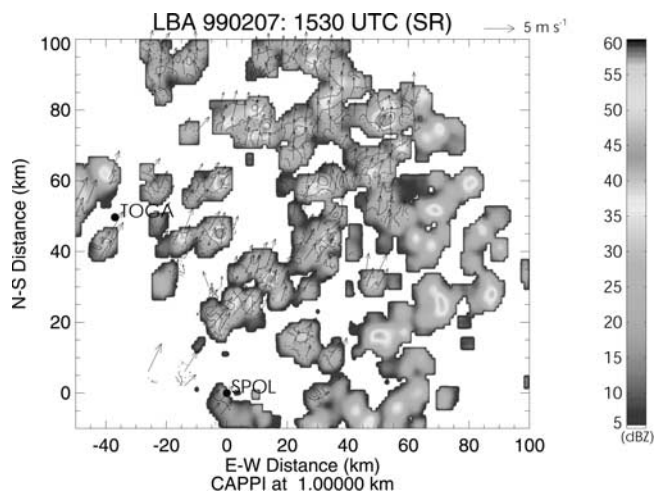


**Figure 9.** Radar CAPPI of reflectivity (shaded), horizontal wind vectors (storm relative), and convergence (contours of  $\pm 0.1$  and  $0.9 \times 10^{-3} \text{ s}^{-1}$ ) at 1530 UTC at a height of 1 km AGL. The locations of the S-POL and TOGA radars are indicated in the plot.

$30^\circ$  toward  $210^\circ$ ); however, the average speed of the line increased from  $5 \text{ m s}^{-1}$  prior to 1710 UTC to approximately  $7 \text{ m s}^{-1}$  after 1710 UTC.

[22] Figure 9 shows the echo features across the sampling domain at 1530 UTC. At this time, the echo population represents a mostly unorganized cumulus field embedded in weak northeasterly flow. The line feature is barely discernible as a loose aggregation of cells in the northeast segment of the plot. By 1630 UTC, this feature had solidified into a linear band with a roughly northwest-southeast orientation. At this point, the band was over 100 km in length, although the width barely exceeded one cell ( $\sim 10 \text{ km}$ ) in many places (Figure 10). Long range surveillance scans (not shown) revealed that a significant portion of the band extended outside (north) of the dual-Doppler domain.

[23] Animation of the low-level CAPPI's showed that the line moved via discrete propagation during the analysis

period, at least as could be discerned from the 10-min resolution of the radar data. As the line moved toward the southwest, new cells formed out ahead of the line ( $\sim 20\text{--}30 \text{ km}$ ) in an orientation roughly parallel to the main linear band. Between 1700 and 1730 UTC, the newer cells out ahead of the line intensified and solidified into another linear feature while the main portion of the band weakened in its wake (Figure 11). The system continued toward the southwest, albeit at a somewhat faster speed ( $7 \text{ m s}^{-1}$ ). The “new” line contained a trailing region of decaying convection (the previous linear band), which broadened the overall feature considerably in many places along the line. Also evident in Figure 11 is another linear feature with similar northwest-southeast orientation about 50 km to the rear (northeast) of the main line band, moving in roughly the same direction. The line continued to move toward the southwest and lengthened to over 200 km, mostly as a consequence of convection along the southern margin (south of S-POL). Despite its length, the band remained rather loosely organized, eventually breaking up into discrete aggregates of cells. The linear feature eventually decayed several hours after the dual-Doppler analysis period, although remnants were detectable for several more hours.

#### 4.1. Time-Height Sections

[24] In order to examine the mesoscale evolution of the convection in terms of kinematic and microphysical properties, the line feature in each synthesis volume was isolated by qualitative inspection of low-level radar CAPPI's (2 km) for the entire analysis period. Composites of the  $u$ ,  $v$ , and  $w$  components of the wind as well as reflectivity for the isolated region were then calculated. Time-height sections of the composite analyses were constructed for the time period 1530–1810 UTC. Because of the two missing radar volumes mentioned above, linear interpolation was used to fill-in the missing time periods and complete the time-height sections.

[25] Throughout the sampling period, the low-level flow (ground relative) was weak and out of the northeast (see Figures 9–11). The CAPPI's in Figures 9–11 show that the strongest low-level flow was to the rear (north-northeast) of

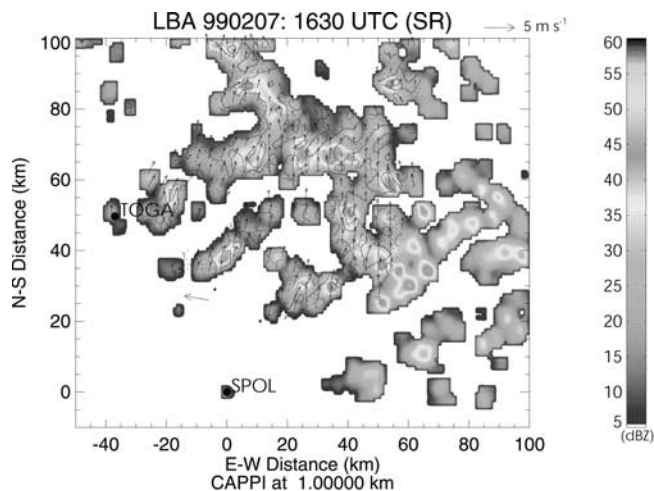


**Figure 10.** Same as Figure 9 except for 1630 UTC.

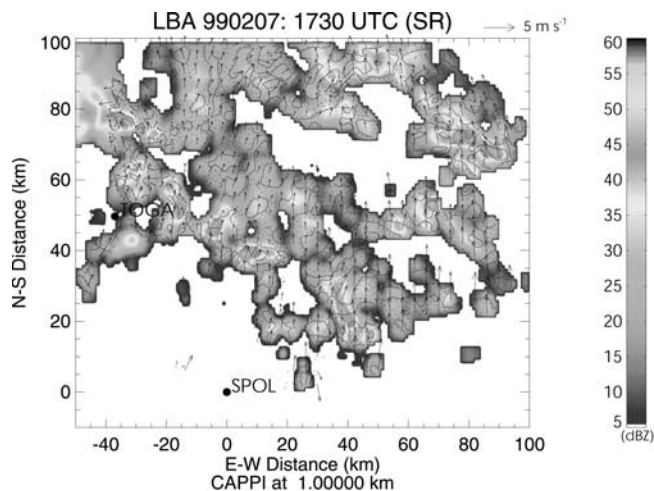


**Figure 11.** Same as Figure 9 except for 1730 UTC.

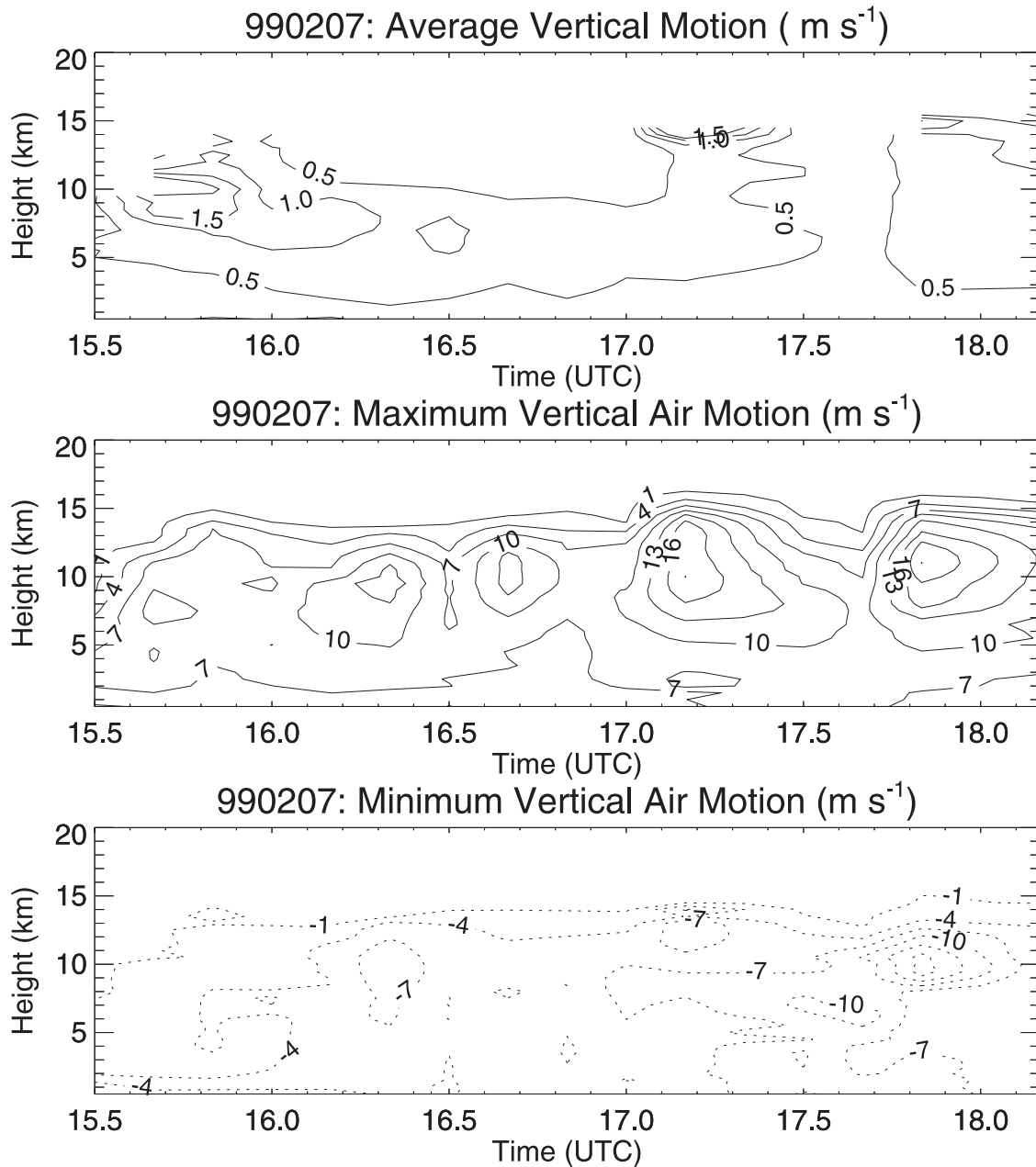


**Figure 12.** Time-height cross-sections of composite vertical air motion (top panel), maximum vertical air motion (middle panel), and minimum vertical air motion (bottom panel) within the region defining the linear band feature in each dual-Doppler synthesis volume. Contour units are  $\text{m s}^{-1}$ . Note change in contour interval between the top and middle-bottom panels. Solid (dashed) contours indicate upward (downward) motion.

the band throughout the sampling period and that there was little curvature, except in the vicinity of convective cores. Figures 12 and 13 show time-height sections of vertical air motion and reflectivity, respectively. Inspection of the maximum vertical air motion and maximum reflectivity panels reveal that the intensity of the system (in terms of depth and magnitude) generally increased over time. However, the intensity modulated several times during the analysis period with each “pulse” being larger than the previous one. Specifically, both the maximum vertical velocity and reflectivity parameters show an increase

in the contour slope at upper levels near 1540 UTC, 1710 UTC, and 1750 UTC (the modulations can also be seen in the average vertical air motion plot). The latter pulse indicates the greatest overall intensity of the line feature during the analysis period with maximum updrafts in at least one cell exceeding  $19 \text{ m s}^{-1}$  near 12 km and the 30 dBZ contour extending to near 11 km. Two other pulses in maximum vertical air motion at 1610 and 1640 UTC are not obvious in the reflectivity cross sections. In general, the reflectivity increased at upper levels over the course of the sampling period as the storm deepened.

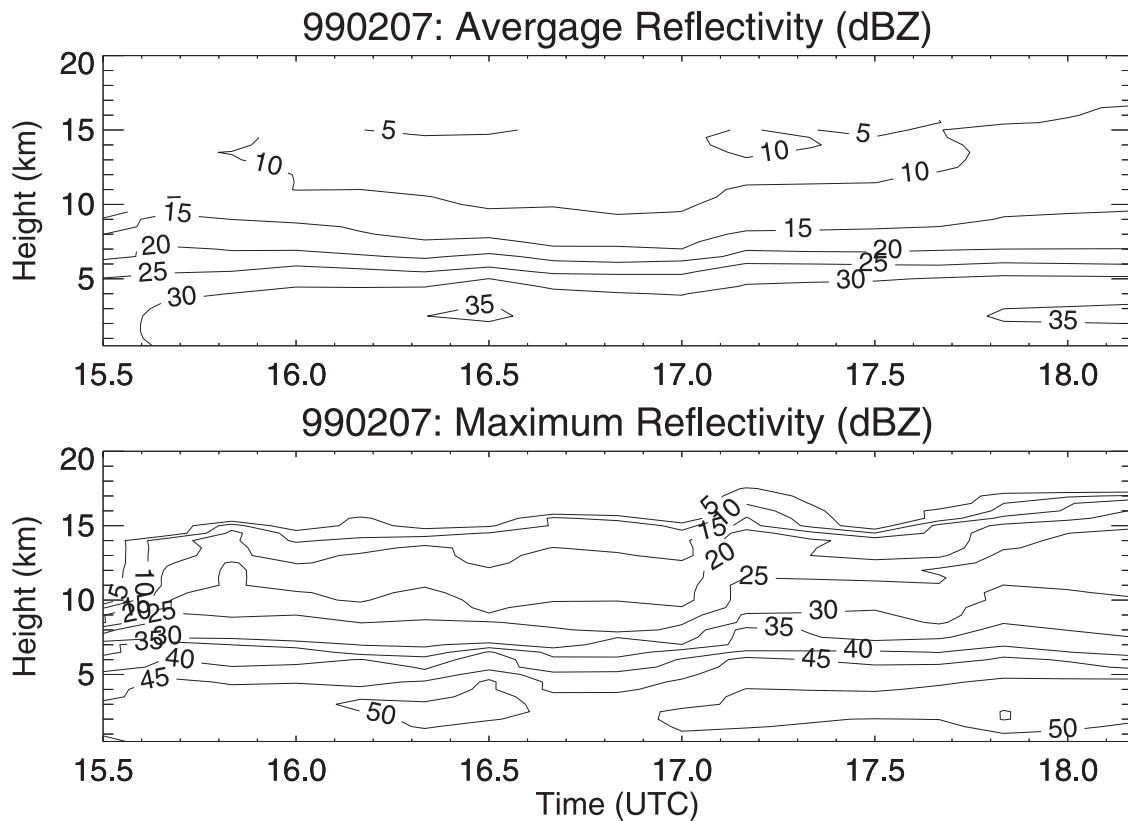


**Figure 13.** Composite reflectivity (top panel) and maximum reflectivity (bottom panel) in the region defining the linear band in each dual-Doppler synthesis. Contour units are dBZ starting at 5 dBZ and incrementing by 5 dBZ.

[26] Figure 14 shows the composite time-height cross section of horizontal wind perpendicular and parallel to the line orientation. The line perpendicular section shows flow from front-to-rear (FTR) at nearly all heights throughout the sampling period. This plot shows that the shear in the lower to middle troposphere decreased over time due to a combination of decreasing FTR below 3 km and increasing FTR between 3 and 9 km. The decrease in low-level FTR is particularly evident after about 17:30 UTC and is probably related to the intensification of new cell growth, and associated convergence, ahead of the line feature (Figure 11). In the upper troposphere, rear-to-front (RTF) flow increased over time, probably due to the overall intensification of the system and subsequent interaction of storm-generated outflow with upper-level easterly flow in the environment.

[27] The storm parallel cross section in Figure 14 shows that the flow is toward the northwest at all heights during the analysis period and that there is significantly larger deep shear (0.5–10 km) parallel to the line compared to the perpendicular direction. Moreover, the storm parallel shear profile does not change substantially over the course of the sampling period.

#### 4.2. Microphysical and Kinematic Vertical Structure of Convection

[28] Convective cells located along the leading edge of the system exhibited an evolving reflectivity structure that was a function of both the stage of lifecycle and the location relative to the edge of the cold pool. During the

early stage of the convective lifecycle, cells developing along the edge of the surging cold pools exhibited a fairly erect vertical structure (Figures 15 and 16). During the mature phase, the convective vertical structure became tilted as the cells extended to heights above the 9-km level (Figures 16 and 17). New cells (Figures 15 and 16) always exhibited first precipitation echoes between the 2- and 4-km height levels. Not surprisingly, multiparameter radar observations indicate that the primary development of rainfall in the growing convection took place via warm-rain processes [e.g., Takahashi, 1990; Bringi *et al.*, 1997; Petersen *et al.*, 1999; Carey and Rutledge, 2000]. This is well illustrated in Figure 15 where a combination of significant differential reflectivities ( $Z_{dr}$ ; e.g., >1 dB) and storm-relative velocity vectors indicate that raindrops formed along the edge of a robust new cell, adjacent to and within an updraft at temperatures well above 0°C. Combined with a 1–2 km spatial offset of significant values of differential propagation phase ( $K_{dp}$ ; > 1°/km), the reflectivity and  $Z_{dr}$  observations<sup>1</sup> suggest that small numbers of large raindrops

<sup>1</sup>Physically,  $Z_{dr}$  is a ratio of the returned power measured at horizontal polarization to that of vertical polarization, and is to the reflectivity-weighted mean particle aspect ratio (e.g., drop oblateness).  $K_{dp}$  is a measure of the difference in phase propagation of the two polarized signals through the medium, and is a combined measure of both liquid water content and mean mass-weighted particle aspect ratio in Rayleigh scattering regimes [cf. Doviak and Zrnic, 1993].

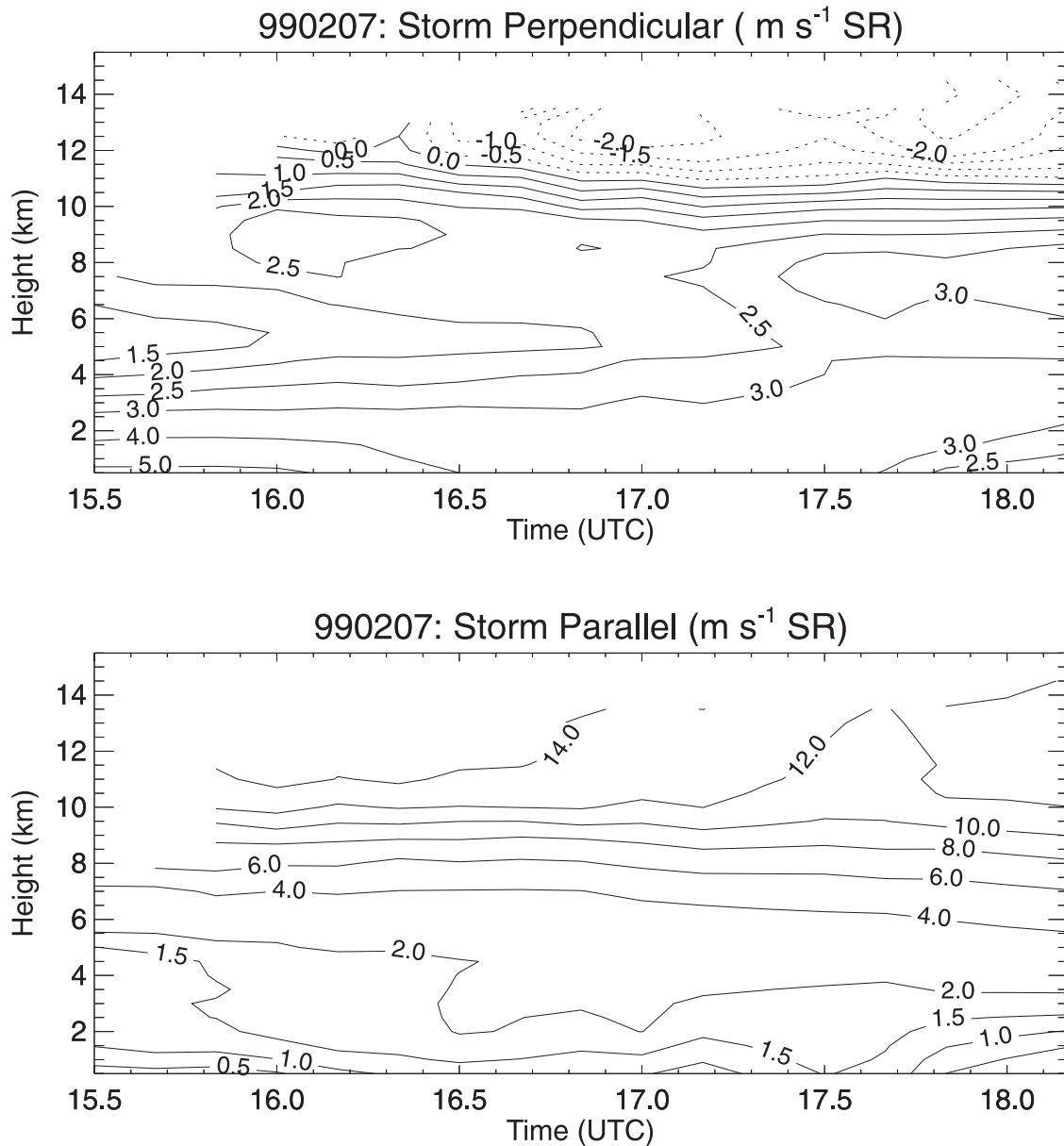


**Figure 14.** Storm relative horizontal wind components perpendicular (top panel) and parallel (bottom panel) to the orientation of the linear band. Units are  $\text{m s}^{-1}$ . Solid (dashed) lines indicate positive (negative) flow. In the top (bottom) panel, flow toward the rear (southwest) is positive.

continued to grow by coalescence as they descended through the updraft, resulting in robust  $Z_{\text{dr}}$  signatures (4 dB; diameter maxima of 5–6 mm) on the edge of the updraft and reflectivity core (Figures 15 and 17). Within the reflectivity cores (Figures 15–17),  $K_{\text{dp}}$  and  $Z_{\text{dr}}$  values suggest the accumulation of an increased rainwater content between the 3 and 4 km levels associated with a larger number of medium sized drops (3–4 mm). These medium-sized drops were also transported laterally as they fell into downdrafts and eventually comprised the bulk of the low-level reflectivity core. Near the 2.5–3 km height level, where local reflectivity maxima were often located (Figures 15–17),  $K_{\text{dp}}$  and  $Z_{\text{dr}}$  values suggest a decreasing liquid water content but slightly larger raindrop diameters (4–5 mm). Drop breakup and evaporation likely explain the

subsequent decrease in both  $K_{\text{dp}}$  and  $Z_{\text{dr}}$  below the reflectivity core and near the surface.

[29] The spatial size sorting of rainfall observed in the cell shown in Figure 15 (reflected in the lateral offset of  $K_{\text{dp}}$  and  $Z_{\text{dr}}$ ), resulted in a pronounced lateral variation of the raindrop size distribution (DSD). This variability in the DSD spanned a distance of approximately 3 km near the surface and was well represented for this particular cell in surface disdrometer measurements of the DSD collected at the Ji Parana airport (not shown).

[30] Representative cross-sections of reflectivity, velocity and polarimetric variables for convective cell types in a mature growth stage are shown in Figures 16 and 17. The more mature cells in Figure 16 (located north of  $y = 25$ ) are typical of the convective intensity and draft structure

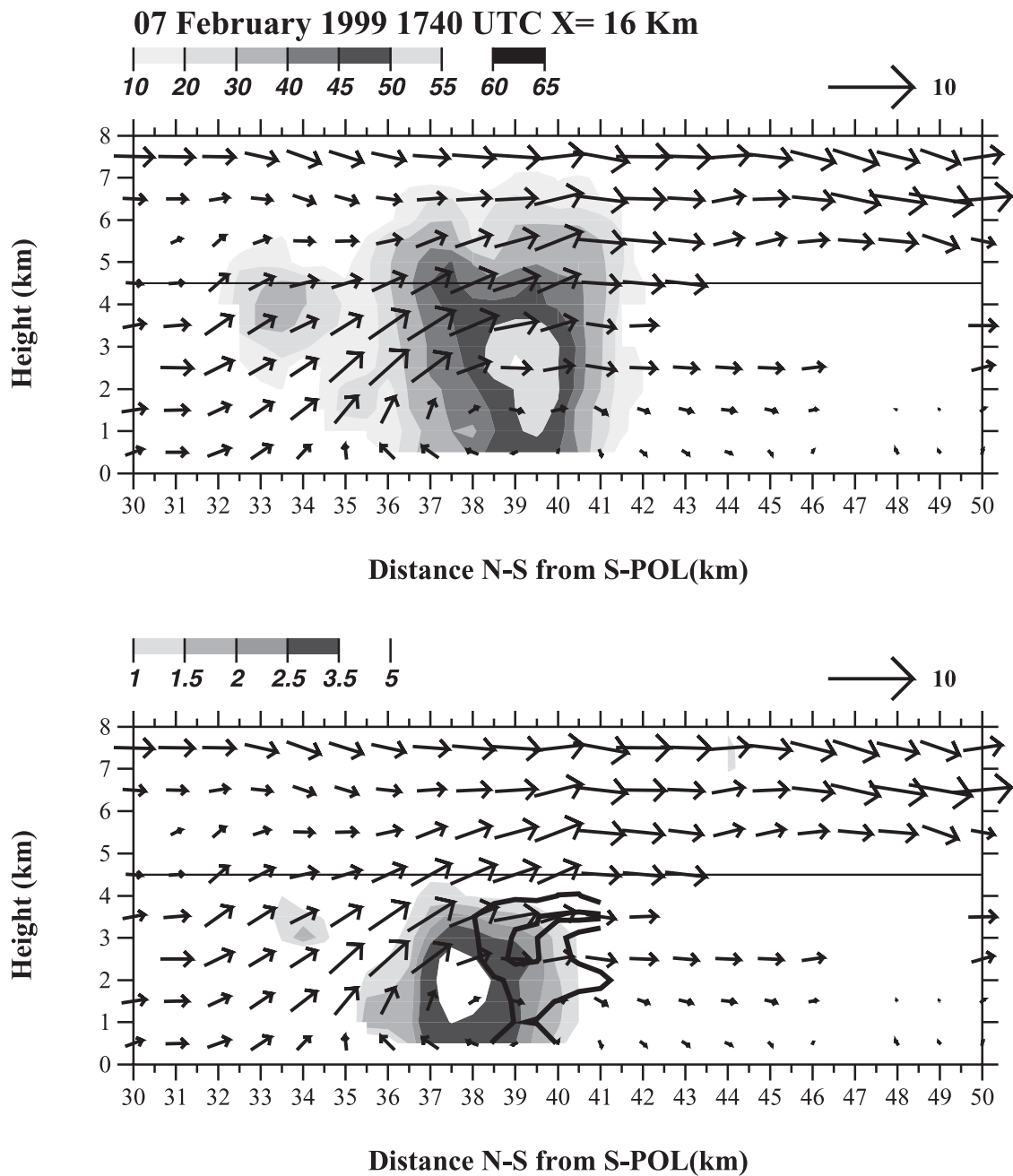


**Figure 15.** 7 February 1999, 1740 UTC. North-south cross section (approximately cross-line) of radar reflectivity and storm relative velocity vectors through a growing cell. a) Radar reflectivity. Values are shaded and vector magnitude is indicated in upper right corner. The solid line indicates the approximate height of the freezing level. b) As in (a) but  $Z_{dr}$  (shaded) and  $K_{dp}$  (contoured every  $1^\circ/\text{km}$  beginning at  $1^\circ/\text{km}$ ).

encountered in this convective system, while the cross section presented in Figure 17 is more representative of the most *intense* convection observed. From a microphysical perspective, one large difference between the deep intense (typical) cells shown in Figures 16 and 17 is the presence (lack) of strong evidence supporting a hail production process in the intense (typical) cell. For the typical or mean cell in this case, the polarimetric radar data suggest that  $Z_{dr}$  columns extending to temperatures  $<0^\circ\text{C}$  accompanied by local enhancements in Linear Depolarization

Ratio (indicating mixed phase processes) were *rarely* observed. Based on previous polarimetric radar studies in the tropics [e.g., *Bringi et al.*, 1997; *Carey and Rutledge*, 2000; *Cifelli et al.*, 2002] this observation suggests that mixed phase processes may not have played as dominant a role in the overall production of rainfall in the system as a whole. Indeed, cloud-to-ground lightning flash counts on this day were at a relative minimum, further supporting the lack of robust mixed phase processes in the clouds. Conversely, as shown in Figure 17, there were at least a few

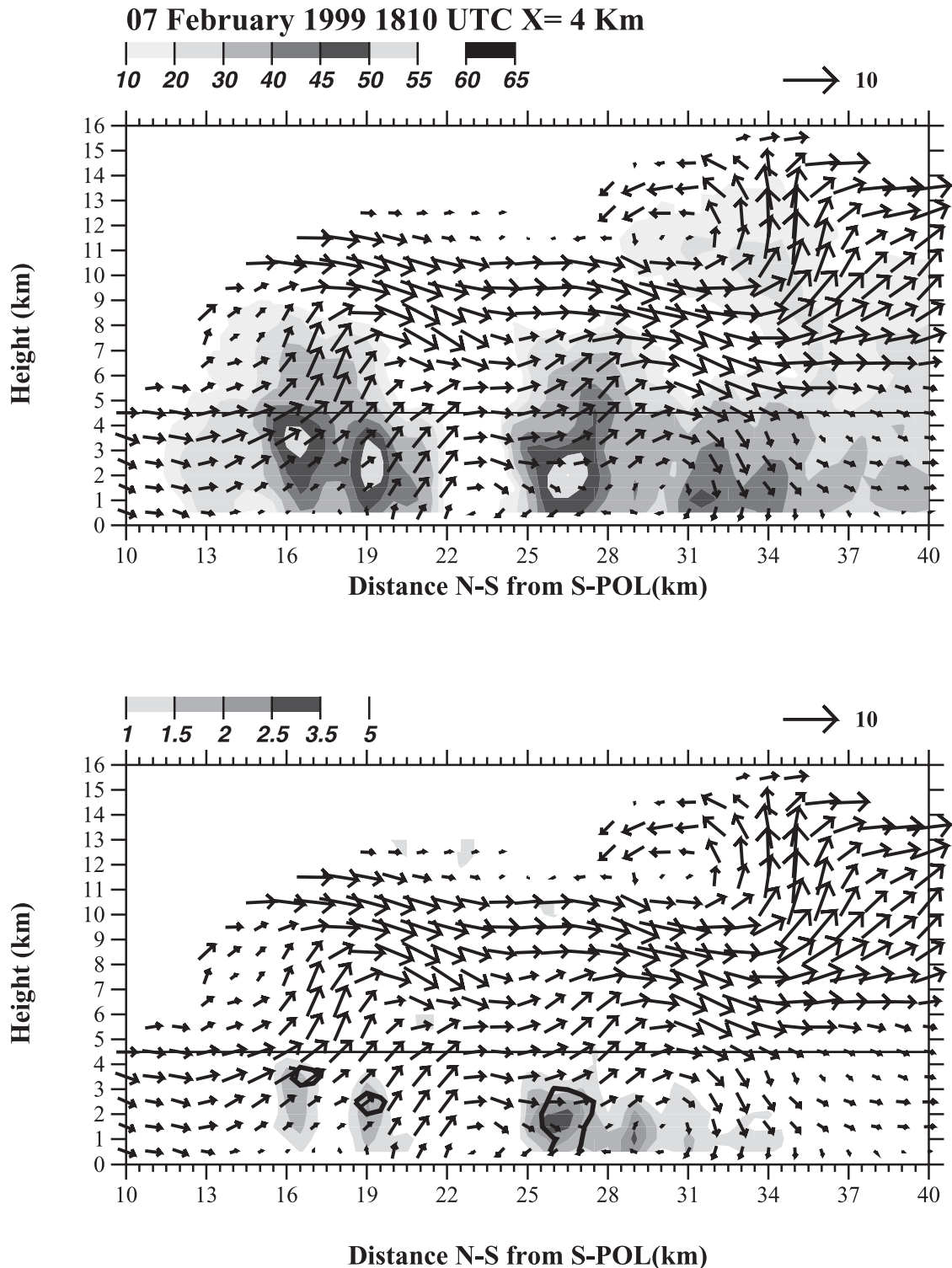


**Figure 16.** 7 February 1999, 1810 UTC. (a) As in Figure 15, but through a mixture of developing and mature convective cells. (b) As in Figure 15.

moderately intense convective cells embedded in the broken line of convection. In these cells significant  $Z_{dr}$  and  $K_{dp}$  were found at temperatures near  $-5^{\circ}\text{C}$  suggesting the presence of a hail process driven by the lofting and subsequent freezing of raindrops. While not the dominant mode of precipitation production in the convective system, it is reasonable to suggest that enhanced downdrafts asso-

ciated with the presence of enhanced ice processes in these cells may have locally enhanced the strength and/or movement of the cold pool along the convective line [e.g., Trier *et al.*, 1996].

[31] From a dynamical perspective, one ubiquitous characteristic of the mature cells was the presence of a discontinuity between low level and upper level updrafts (Figures 16

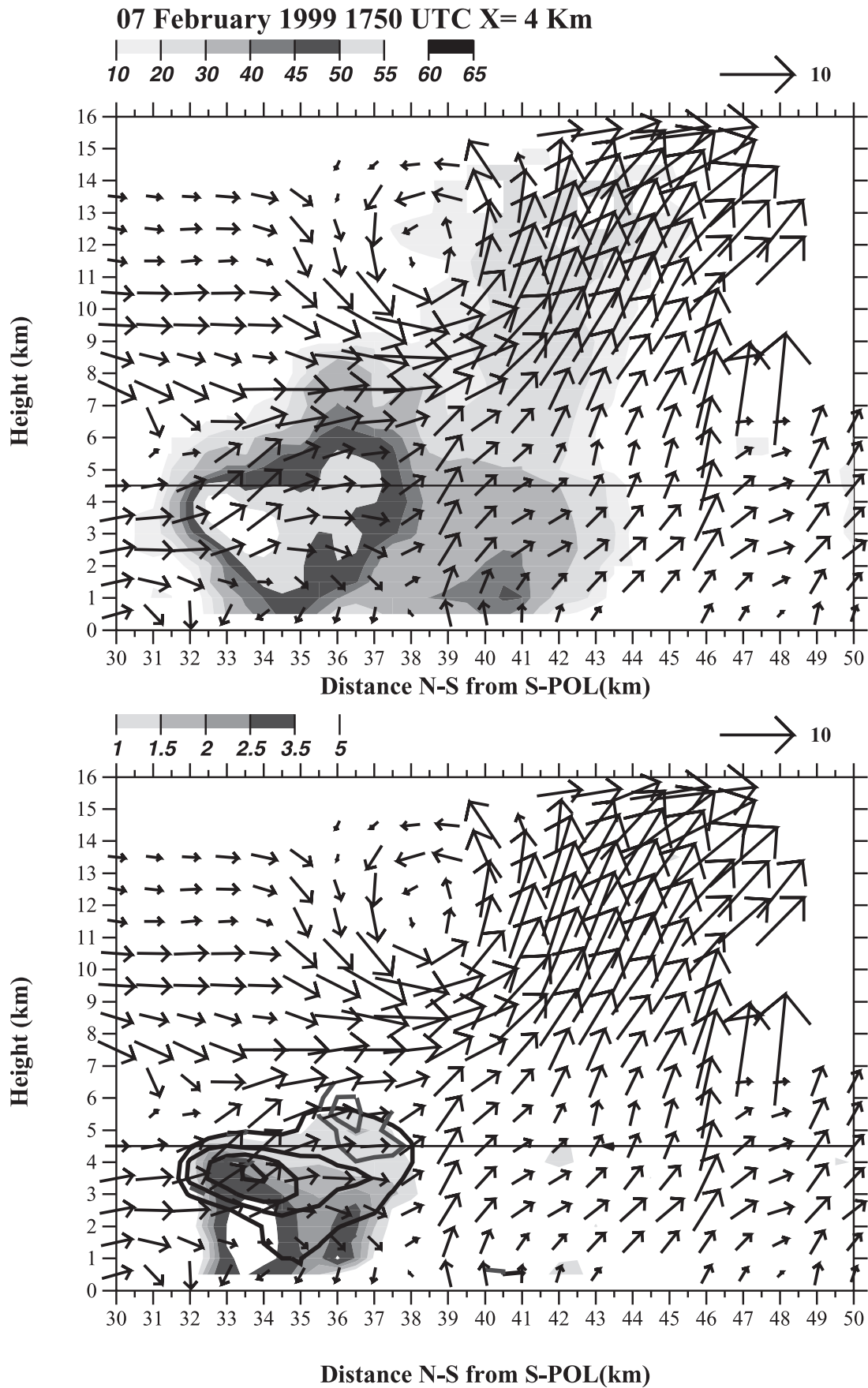


**Figure 17.** 7 February 1999, 1750 UTC. (a) As in Figure 15, but through an intense convective cell. (b) As in Figure 15 except LDR is also contoured (dark gray; interval 1 dB beginning at  $-22$  dB).

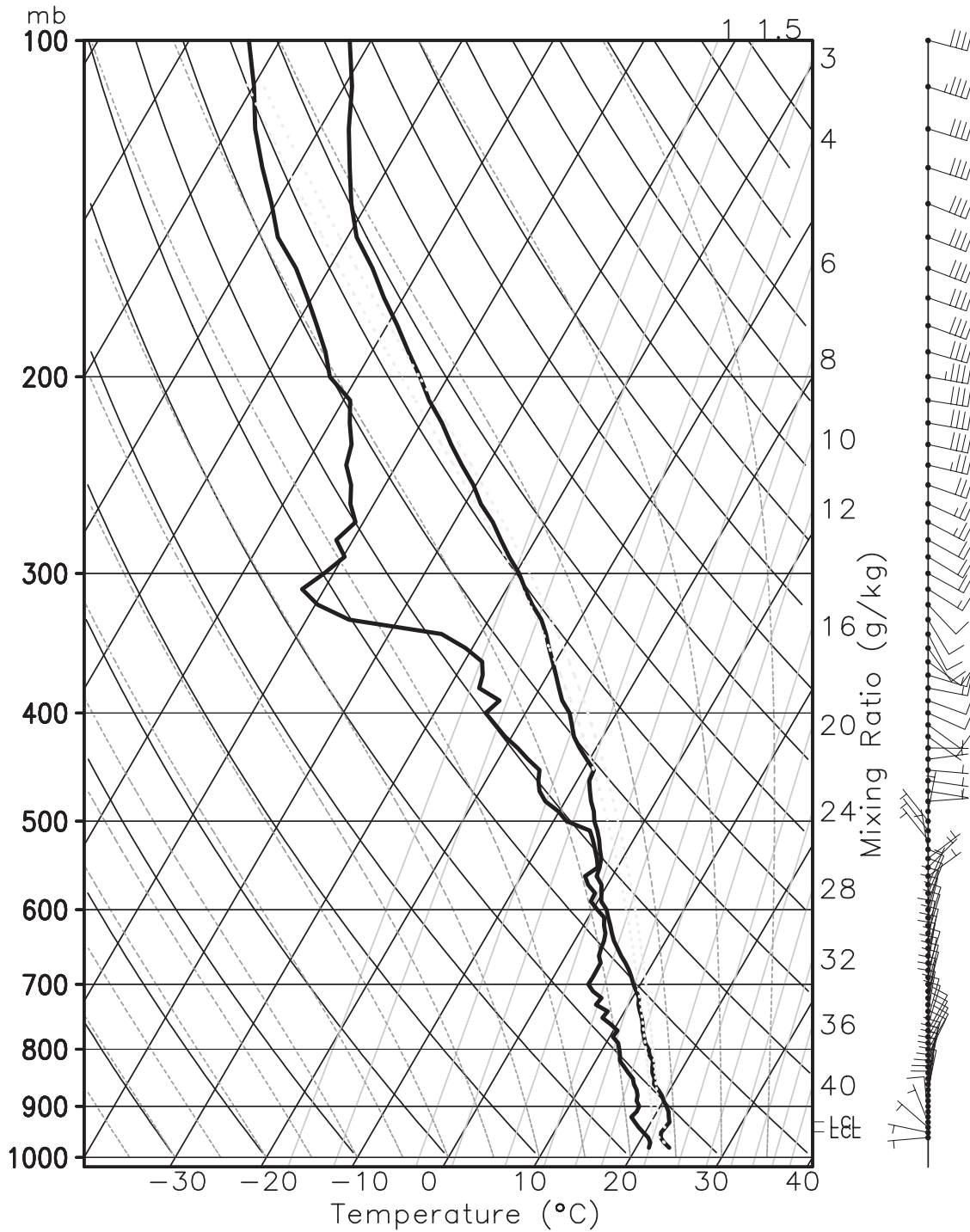


**Figure 18.** Sounding at Rolim de Moura, 7 Feb. 1999, 12 UTC.

and 17). The radar data suggest that as cells developed and deepened, updrafts at mid and upper-levels accelerated as precipitation was unloaded. At the same time, the updrafts at mid levels were progressively displaced northward (in a storm relative sense) from the lower level core. This northward displacement was due to a combination of discrete propagation of the convective system (e.g., cold pool surges that out ran growing convection) and strong upper-level shear. The net effect was to tilt the system rearward and to weaken the precipitation structure at upper levels as the

updraft became cutoff from its vapor/condensate source at lower levels. Enhanced convergence and entrainment of dryer air into the updraft aloft also served to prohibit the growth of large precipitation particles at mid levels. Further, as the strong updrafts in the deeper cells (Figures 16 and 17) impinged on the base of the tropopause, robust overturning circulations appeared on the leading edge of the updraft, resulting in strong dynamically forced downdrafts at mid and upper levels that worked to suppress growing convective towers located along the new location

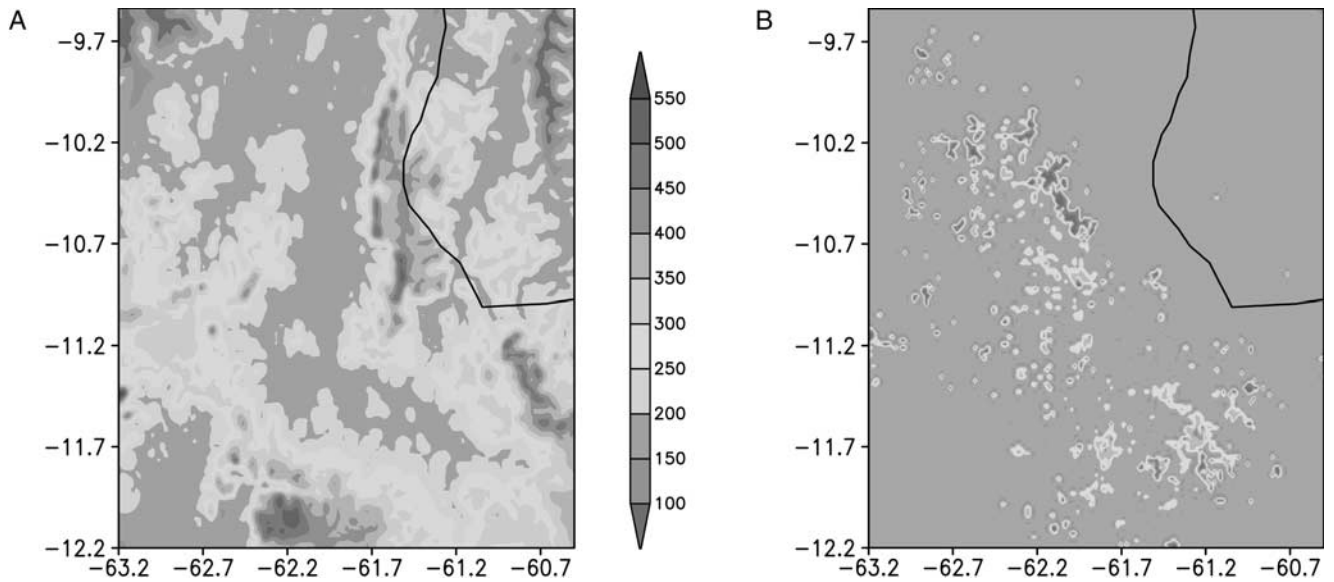


**Figure 19.** Topography (left) and vegetation class (blue is evergreen broadleaf trees and the other colors are related either to grassland, shrubs, farming areas).

of the cold pool (Figures 16 and 17). In fact, the data suggest that downdrafts driven by the mid and upper level convergence associated with the overturning circulation may have, in some instances, merged with lower level downdrafts to form a deep column of subsidence and associated precipitation free zones (e.g., Figure 16) between new convection on the edge of the surging cold pool and the old position of the convective line (similar to the presence at upper levels of a dynamically forced transition region in a squall-line) [e.g., *Biggerstaff and Houze, 1993*]. Coupled with discrete jumps in cold pool position, this process would serve to isolate convection in old convective lines from the new, resulting in the appearance of multiple convective lines.

**5. Numerical Simulation**

[32] A nested grid approach with nudging toward a large-scale analysis and to observed data was tried with 3 grids, with resolutions of 32, 8, and 2 km, starting several days before. The main problem with this run was that simulated clouds and rainfall were seen to develop and dissipate, and several persist through the morning of 7 February, giving unrealistic initial conditions for that particular day. The soil moisture evolves according to the simulated rainfall giving also a distribution that may be coherent with the simulation but is not coherent with the previous day and night observed rainfall. In order to start from an initial condition more realistic the horizontally homogeneous run presented a better option, in this case. For the soil moisture the adjustment consisted in increase it until the surface temperature evolution and the mixed layer heights in the model and in the observations during the morning, in the pasture site, were similar. The forest site was less sensitive to the evolution of soil moisture in the upper layers since the roots remove water from deeper layers which have always plenty of water. A vertical profile of soil moisture, drier at the surface and moister at the bottom of the soil model, induces a horizontal variability in the portioning of surface

fluxes through the deeper roots of vegetation in the forest and shallow roots in deforested areas. Using a homogeneous run may then be justified for this particular day as a means to analyze the effect of the surface in the absence of large-

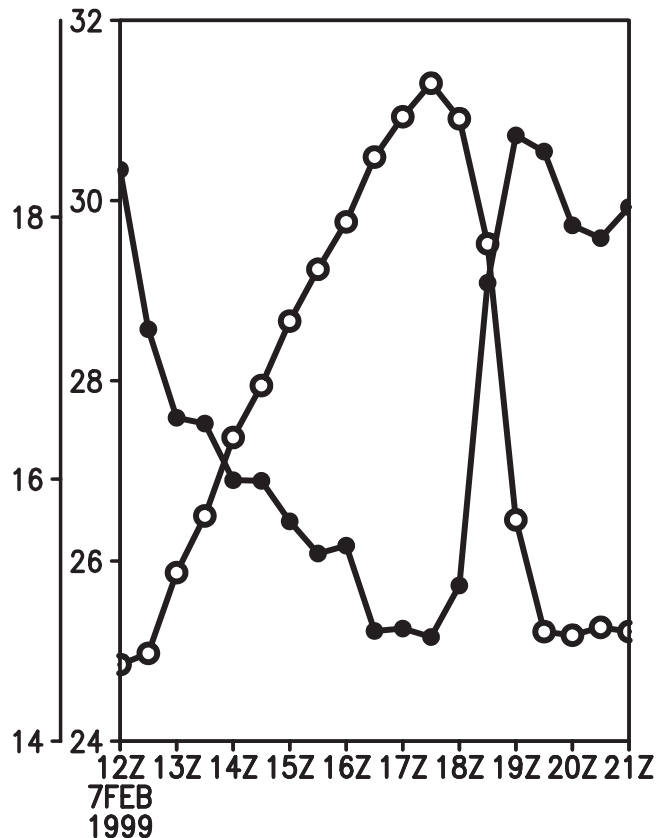


**Figure 20.** Simulated temperature T (open circles in °C) and water vapor mixing ratio (r - closed circles in  $g\ kg^{-1}$ ) for a deforested grid point (close to ABRACOS site) for the control run.

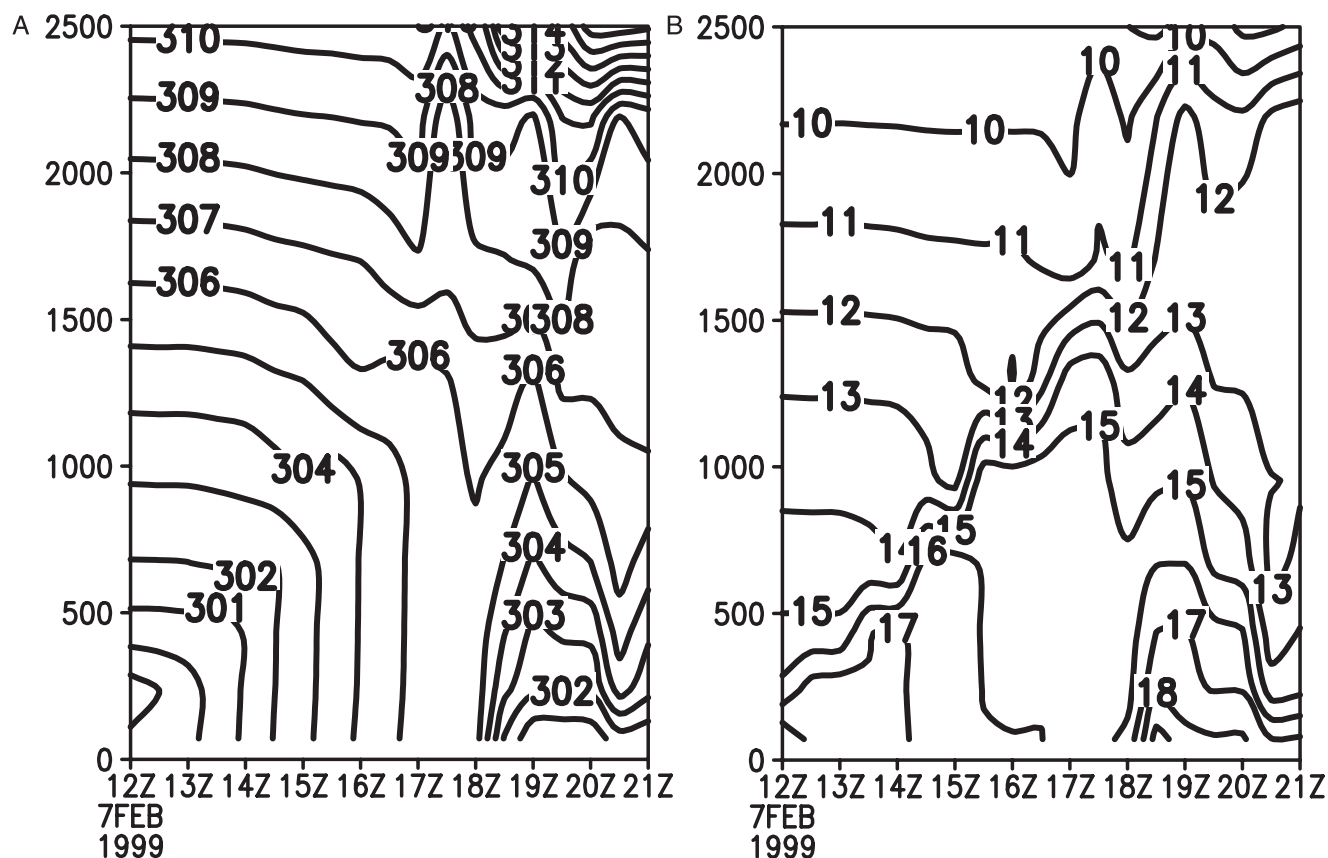


**Figure 21.** Simulated evolution of potential temperature and water vapor mixing ratio at 10.8 S 62 W for the control run.

scale forcing and because most of the area under analysis was actually clear during the morning.

[33] The objective of the numerical simulations is to evaluate the impact of dynamic instabilities versus surface forcing (topography and land cover) in the development of a convective line. Three simulations will be discussed here: (1) control run (with all the options presented in section 2); (2) flat run with inhomogeneous vegetation and (3) homogeneous vegetation (forest) run with real topography. The flat run differs from the control run in the topography which is uniform throughout the model domain with an altitude of 225 m. The impact of topography may be seen by comparing the control run and the flat run. The impact of deforestation may be addressed comparing the control run and the forest run. Before discussing the differences between the three runs, a brief description of the time and spatial evolution of the convective activity in the control run will be presented.

[34] The sounding at Rolim de Moura used to initialize the model may be seen in Figure 18. It shows a typical moist sounding with northwesterlies in the lower levels and easterlies in the upper levels in accordance with the large-scale situation depicted in Figure 2. A saturated layer between 500 hPa and 600 hPa did not persist through the morning hours and did not seem to have an impact on the model evolution. The topography and vegetation classes may be seen in Figure 19 and show that the deforested area (forest is blue and other colors indicate deforested areas) lies in the diagonal of the domain mostly under heights of 250 m. Most of the area with altitudes higher than 250 m

is covered by forest. In the western half the terrain height is seen to gradually increase from north to south while in the eastern half a north south mountain range with altitudes reaching 500 m is the dominant feature with well defined valleys to the east and west. The eastern edge of the deforested area actually reaches the bottom of the valley at the Machado River; to the east of the river, terrain gradually gets higher and is covered by forest.

[35] The soil moisture has been used to tune the depth of the mixed layer and the diurnal temperature variation to the observed values at the ABRACOS site. Figure 20 shows the modeled temperature and water vapor mixing ratio at the first model level which is located at 71 m above the surface. These values should be compared to Figure 4 taking into account that the latter are surface values so that a difference of about 1°C during daytime is expected from an adiabatic mixed layer. Taking this into account the temperature is seen to vary in both figures from about 25 to 32°C and a temperature drop of about 7°C is seen in the observations at 1800 UTC and about one hour later in the model run. The evolution of the vertical profile of potential temperature and water vapor mixing ratio in the control run for a typical point in the deforested area may be seen in Figure 21 and compared to Figure 3. Again, model and observations are similar with about 1 hour lag in the features associated to the convective line passage, i.e., the break in mixed layer growth associated to the downward transport of high potential temperature values and low mixed layer values. Near the surface, potential temperature falls and mixing ratio increases just after the

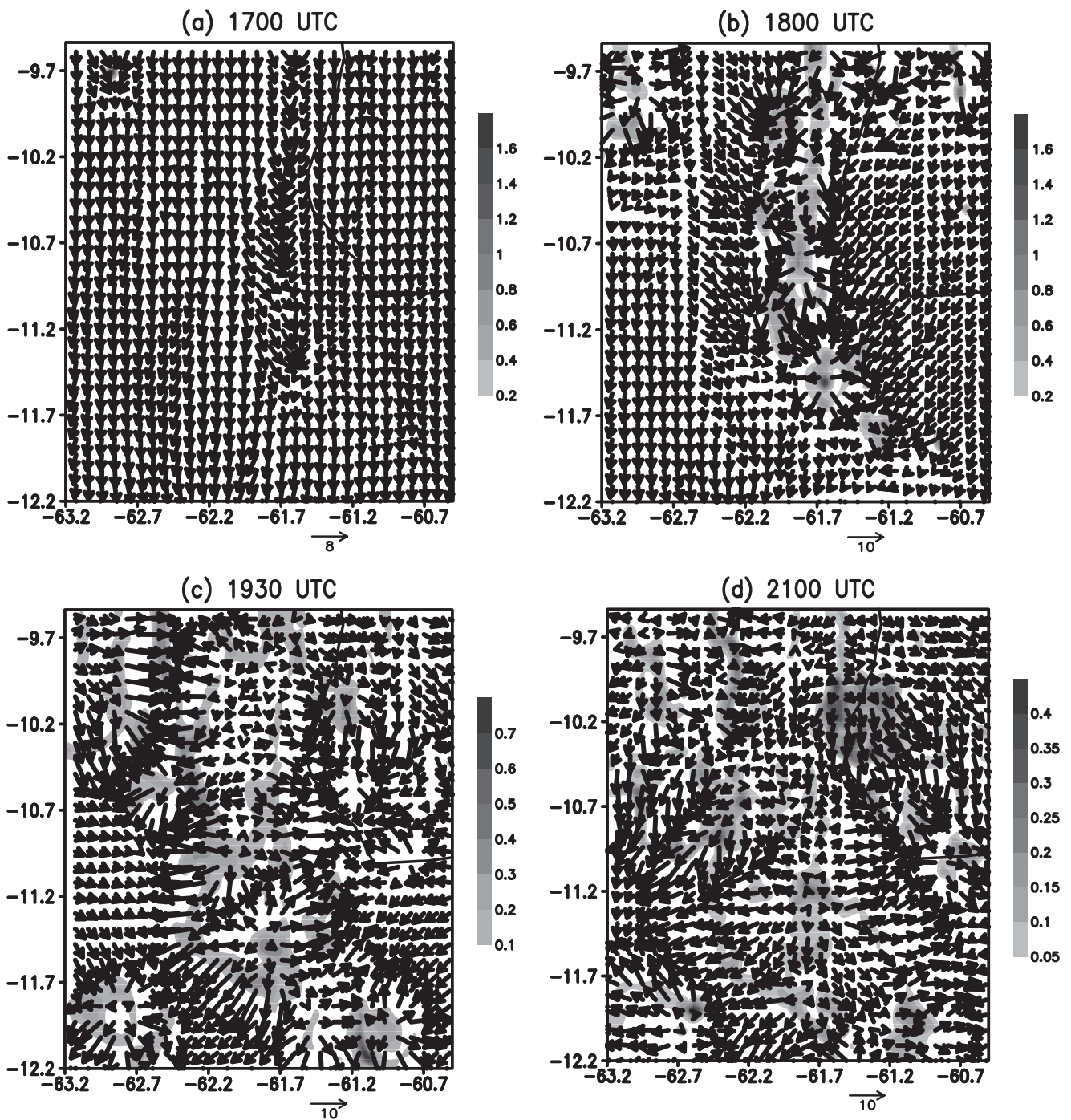


**Figure 22.** Rainwater mixing ratio ( $\text{g kg}^{-1}$ ) and wind vectors at 71 m AGL (wind vectors plotted at every 6th grid point).

line passage followed by a decrease in mixing ratio in a similar fashion as described in section 4.

[36] To achieve the agreement in mixed layer depth growth during the morning the soil type used has been a sandy clay loam with 5 levels from the surface to 2 m depth with soil moisture of 39% saturation at the first level below the surface and increasing linearly to the deepest level to 45%. Since there is no memory from the previous day convective activity, in the form of heterogeneous soil moisture at the initial time, some differences in convective

development may be expected, perhaps even explaining the timing of the convective line development in the model. The homogeneous initialization of meteorological variables may also have an impact in the development of the convective system.

### 5.1. Control Run

[37] Figure 22 shows the rainwater mixing ratio and the wind fields at 71 m AGL. At 1700 UTC the first rain cells are seen over the north-south mountain range at about  $61.7^\circ\text{W}$

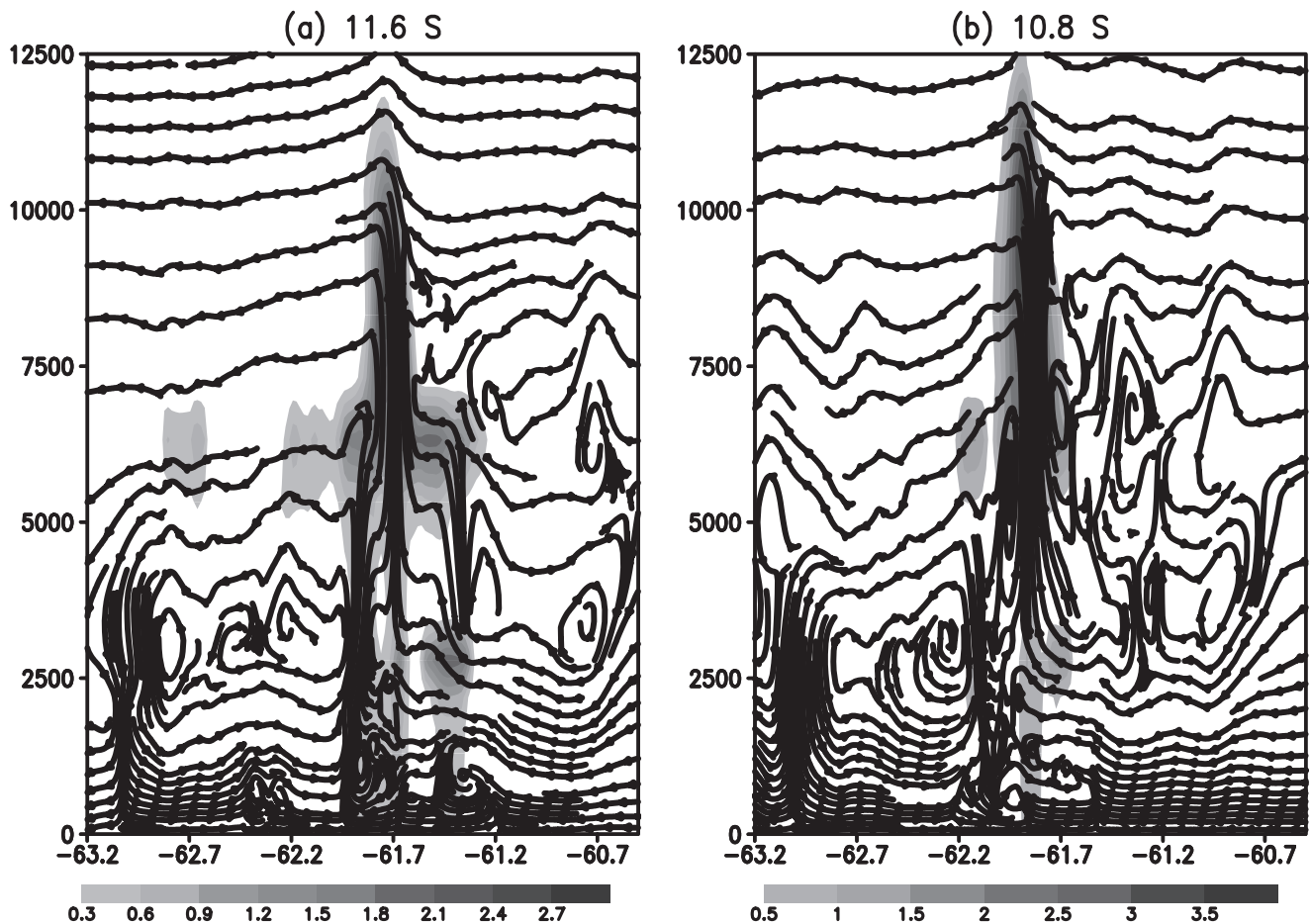


**Figure 23.** Height  $\times$  longitude cross section of total mixing ratio of all condensate (water and ice) and streamlines ( $u, w$ ) at 1830 UTC.

(cf. Figure 19 for the topography); it is important to note at the southern edge of the mountain range the development of a cell that in the next hour becomes the precursor of a convective line. Well organized outflow boundaries originated from the downdrafts are seen to gradually organize the rain cells. At 1800 UTC the rain has moved west of the mountain range and the cell to its south becomes larger. At 1930 UTC the line to the south has a NW to SE orientation and new cells are seen again in the northern part of the mountain range building up a new convective line. Comparing this evolution with the radar observations, it may be seen that Figure 9, although at an earlier time (about 1 hr), shows a line of echoes around the 60-km N-S range mark that corresponds to the location of the mountain range. Figures 10 and 11 also show the new cell in the northern part, building up into a new convective line.

[38] *Alexander and Young* [1992] and *LeMone et al.* [1998] analyze the evolution of tropical convective lines and found that in the case of weak low level shear the lines were oriented parallel to the midlevel shear. Accordingly, in the present case, the mid level shear between 800 and 400 hPa, from the wind profile in Figure 18, is from  $122^\circ$ , i.e., basically from the SE.

[39] Following the convective line motion, a propagation speed of about  $10\text{--}11\text{ m s}^{-1}$  is found which is faster than the observed  $5\text{--}7\text{ m s}^{-1}$ . The vertical structure of the

convective cells may be seen in Figure 23 as a cross section at  $11.6^\circ\text{S}$ ,  $10.8^\circ\text{S}$ , and  $10.3^\circ\text{S}$ . The deepest cells reach 12–14 km with maximum condensate mixing ratio between 3 and  $4\text{ g.kg}^{-1}$ . It is seen that the upper level updraft lags behind the low level updraft with a tilt similar to the one seen for the radar profiles in Figures 16 and 17. The discrete propagation indicated in section 4 is seen also in the numerical simulation as new cells developing ahead of the deep ones in Figures 23a and 23b. However, just a few cells are deep, consistent with the radar observations, most of the condensate remains below 7000 m for most of the extension of the line. Ice water content at 9300 m AGL may be seen in Figure 24 for several times indicating that only two cells of the initial line have significant ice content at this level and that the line formed over the topography in later times also originates from a deep cell with ice water content in upper levels. Vertical speeds in the model never exceed  $13\text{ m s}^{-1}$ , below the radar derived vertical wind speeds (up to  $19\text{ m s}^{-1}$ ). However, model output has been obtained for every half hour and larger values might be found between output times. Rainfall rates of 33 mm in 30 min are seen in the simulation at the early stages between 1730 UTC and 1830 UTC. The rainfall rates in Figure 8 are 5 min rates but are coherent with the simulated results. Wind gusts in Figure 4 show values reaching  $20\text{ m s}^{-1}$  while the wind speed in the numerical simulation does not exceed  $14\text{ m s}^{-1}$ .

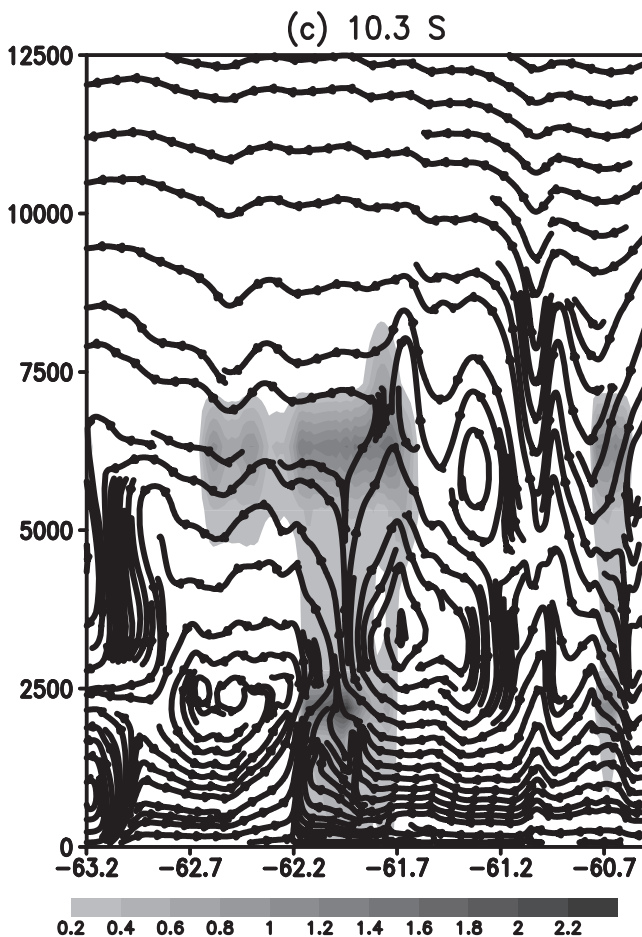


Figure 23. (continued)

[40] As a summary, the simulated convective lines are seen as a result of convective cells that start over the N-S mountain range about one hour later than in the observations, move faster and seem less vigorous than the observations. On the other hand, there is a reasonable similarity in the depth, overall orientation, rainfall rates and evolution of outflow boundaries and even on the later development of a new line on the northern part on the mountain range. The radar observations suggesting that only a few cells were intense and had large ice water content in their upper half is also obtained in the simulation. It is seen that, although not perfect, the simulation captured some basic features of the observations and can therefore serve as a basis for the discussion in the next section.

[41] The different time of convection start might have an impact on the strength of convection given, for example, by the maximum simulated updrafts. The effect of the initial sounding has been only in the moisture deficit: too moist soundings develop a stratus deck in the simulation that prevents surface heating until dissipation thus unrealistically postponing the diurnal cycle of temperature and moisture at the surface. The sounding used appears to be quite representative of the area at the initial time. Different options in the microphysics parameterization of RAMS essentially reproduce the overall convective evolution with a  $\pm 20\%$  difference in intensity. Further studies are needed, however, in order to fully explore the role of cloud condensation

nuclei in the microphysics of clouds in the Amazon region as suggested by *Silva Dias et al.* [2002].

## 5.2. Impact of Topography and Vegetation Contrast

[42] The differences in location and intensity of surface rainfall between 1730 and 1800 UTC may be seen in Figure 25 for the three runs. At this initial stage the cells are more north south oriented than later (cf. Figure 22). Topography is seen as a fundamental forcing for the location of the first cells in the model; in the flat run, cells are randomly formed except for a line of cells in the eastern edge of the deforested area in the valley. The cell at the south end of the mountain range is more confined in the forest run and maximum rainfall rate is seen in the flat run. The domain average temporal evolution of precipitation (not shown) for the three runs indicate that the flat run has the maximum average precipitation rate in 30 min although it starts later than the other two and has a shorter duration. The control run has more rainfall than the forest run. The average over all domain precipitation total for the duration of the simulation (12 hours) is 11.3, 9.5 and 10.2 mm for the control, flat and forest runs, respectively. The average precipitation for 7 February from the rain-gages in Figure 8, is 15.7 mm.

## 6. Conclusion

[43] The merging picture from a combination of data analysis and numerical simulations for the 7 February convective development in Rondônia may be summarized as follows. In the absence of large-scale forcing on a clear and sunny morning, shallow convective cells are seen to form all over the area and deep cells develop over the N-S mountain range where enhanced sensible heat flux [*Souza et al.*, 2001] favors early development. In this particular synoptic situation of low level northwesterly flow, enhanced convergence and more vigorous convective cells (if formed) are favored on the southern end of the north-south mountain range. The subsequent evolution is seen as a result of spreading outflows formed by downdrafts of the more intense cells where ice processes are active and cloud tops reach the upper troposphere. Gust fronts are seen to be initially moist, but gradually become drier as downdrafts from about 80–90 hPa above cloud base reach the surface.

[44] The radar data suggest that as cells developed and deepened, updrafts at mid and upper-levels accelerated as precipitation was unloaded. At the same time, the updrafts at mid levels were progressively displaced northward from the lower level core. The net effect was to tilt the system rearward and to weaken the precipitation structure at upper levels as the updraft became cutoff from its vapor/condensate source at lower levels. Enhanced convergence and entrainment of dryer air into the updraft aloft also served to prohibit the growth of large precipitation particles at mid levels. Further, as the strong updrafts in the deeper cells impinged on the base of the tropopause, robust overturning circulations appeared on the leading edge of the updraft, resulting in strong dynamically forced downdrafts at mid and upper levels that worked to suppress growing convective towers located along the new location of the cold pool. In fact, the data suggest that downdrafts driven by the mid

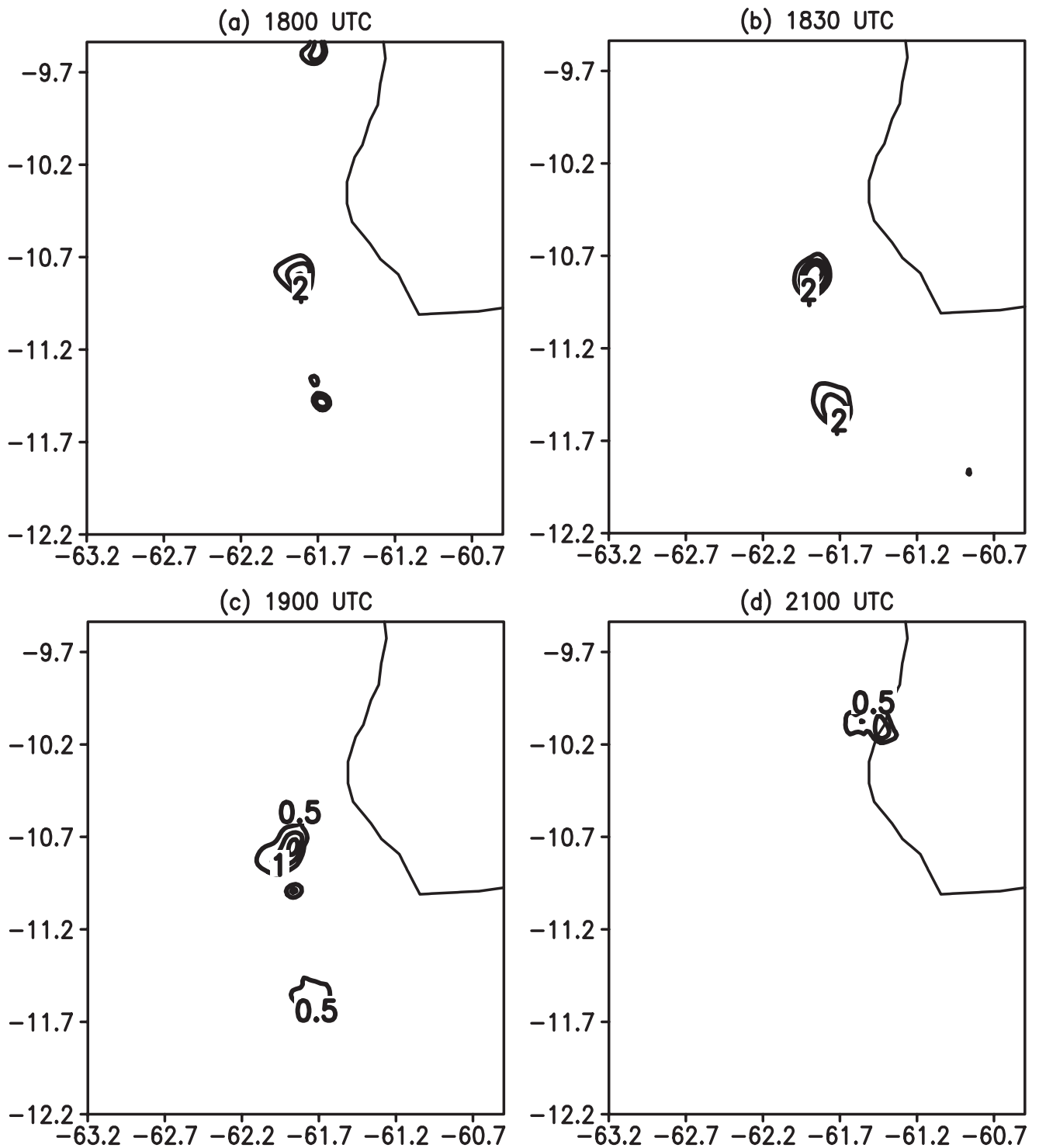
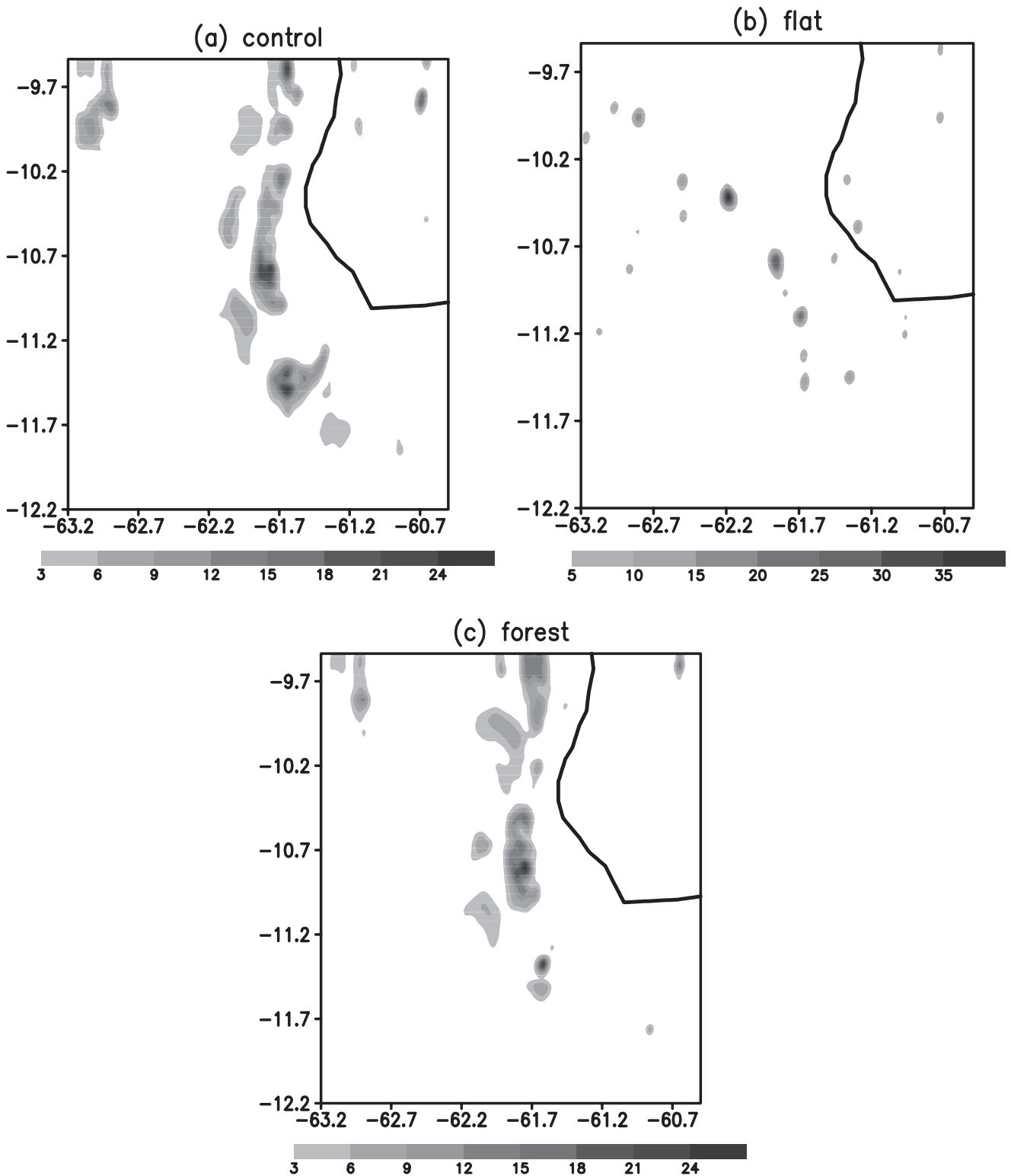


Figure 24. Total ice water content at 9300 m in  $\text{g kg}^{-1}$  (control run).

and upper level convergence associated with the overturning circulation may have, in some instances, merged with lower level downdrafts to form a deep column of subsidence and associated precipitation free zones between new convection on the edge of the surging cold pool and the old position of the convective line. Coupled with discrete jumps in cold pool position, this process would serve to isolate convection in old convective lines from the new, resulting in the appearance of multiple convective lines.

[45] The effect of deforestation has been analyzed in this particular case from a numerical model perspective and is seen to enhance total rainfall over the area. *Nobre et al.* [1991] discussed the effect of an overall deforestation over the Amazon region consisting of a complete change of forest into pasture areas showing that the net effect would be a reduction in total rainfall and increase in surface temperature. *Silva Dias and Regnier* [1996] showed that in the dry season, enhanced vertical motion would be



**Figure 25.** Ground precipitation (in mm/30 min) between 1730 and 1800 UTC for (a) control run; (b) flat run; (c) forest run.

expected over the deforested areas in Rondônia thus explaining the satellite observations in *Cutrim et al.* [1995] that showed enhanced shallow cumulus clouds over deforested areas as well as over mountain ranges, again for the dry season. *Wang et al.* [2000] discuss the effect of deforestation in the rainy season in Rondônia in a situation of strong large-

scale forcing and found no impact. However, the rainy season in Rondônia as shown by Rickenback et al. (submitted manuscript, 2001) undergoes phases where the large scale dominates, convection is widespread and the diurnal cycle is not so strong as during the phase where there is no large-scale forcing. In the latter, the surface processes are

dominant. In the present case of very weak large-scale forcing a preference for deep cloud development over the mountains is suggested and deforestation may be acting as an enhancing factor for total rainfall. Clearly, there is a limit to the potential increase in rainfall in association with deforestation since, eventually, drier air may hinder further convective development.

[46] **Acknowledgments.** Acknowledgments are due the NASA/TRMM Program Grants NAG5-9642 and NCC5-288 and the Fundação de Amparo à Pesquisa do Estado de São Paulo - FAPESP Grant 1997/9926-9. Support from the European Community (LBA-EUSTACH) and Netherlands Research Program Global Air Pollution and Climate Change are acknowledged. The National Science Foundation partially supported the S-POL radar deployment. Many thanks to all the Brazilian, American, and European participants of the field experiment. Thanks are also due to CNPq/MCT who provided scholarships for many LBA participants.

## References

- Alexander, G. D., and G. S. Young, The relationship between EMEX mesoscale precipitation feature properties and their environmental characteristics, *Mon. Weather Rev.*, *120*(4), 554–564, 1992.
- Betts, A. K., Boundary layer thermodynamics of a High Plains severe storm, *Mon. Weather Rev.*, *112*, 2199–2211, 1984.
- Betts, A. K., J. D. Fuentes, M. Garstang, and J. H. Ball, Surface diurnal cycle and boundary layer structure over Rondônia during the rainy season, *J. Geophys. Res.*, *107*, 10.1029/2000JD000356, in press, 2002a.
- Betts, A. K., L. V. Gatti, A. M. Cordova, M. A. F. Silva Dias, and J. Fuentes, Transport of ozone to the surface by downdrafts at night, *J. Geophys. Res.*, *107*, 10.1029/2000JD000158, in press, 2002b.
- Biggerstaff, M. I., and R. A. Houze, Kinematics and microphysics of the transition zone of the 10–11 June 1985 squall line, *J. Atmos. Sci.*, *50*, 3091–3110, 1993.
- Bringi, V. N., K. Knupp, A. Detwiler, L. Liu, I. J. Caylor, and R. A. Black, Evolution of a Florida thunderstorm during the Convection and Precipitation/Electrification Experiment: The case of 9 August 1991, *Mon. Weather Rev.*, *125*, 2131–2160, 1997.
- Carey, L. D., and S. A. Rutledge, The relationship between precipitation and lightning in tropical island convection: A C-band polarimetric radar study, *Mon. Weather Rev.*, *128*, 2687–2710, 2000.
- Carey, L. D., S. A. Rutledge, D. A. Ahijevych, and T. D. Keenan, Correcting propagation effects in C-band polarimetric radar observations of tropical convection using differential propagation phase, *J. Appl. Meteorol.*, *39*, 1405–1433, 2000.
- Carvalho, L. M. U., and C. Jones, A satellite method to identify structural properties of mesoscale convective systems based on the maximum spatial correlation tracking technique (MASCOTTE), *J. Appl. Meteorol.*, *40*, 1683–1701, 2001.
- Cifelli, R., W. A. Petersen, L. D. Carey, S. A. Rutledge, and M. A. F. Silva Dias, Radar observations of kinematic, microphysical, and precipitation characteristics of two MCSs in TRMM LBA, *J. Geophys. Res.*, *107*, 10.1029/2000JD000264, in press, 2002.
- Cohen, J. C. P., M. A. F. Silva Dias, and C. A. Nobre, Environmental conditions associated with Amazonian squall lines: A case study, *Mon. Weather Rev.*, *123*(11), 3163–3174, 1995.
- Cutrim, E., D. W. Martin, and R. Rabin, Enhancement of cumulus clouds over deforested lands in Amazonia, *Bull. Am. Meteorol. Soc.*, *76*(10), 1801–1805, 1995.
- Doviak, R. J., and D. S. Zrnic, *Doppler Radar and Weather Observations*, Academic, San Diego, Calif., 562 pp., 1993.
- Garstang, M., L. H. Massier Jr., J. Halverson, S. Greco, and J. Scala, Amazon coastal squall lines, Part I, Structure and kinematics, *Mon. Weather Rev.*, *122*, 608–622, 1994.
- Gash, J. H., C. A. Nobre, J. M. Roberts, and R. L. Victoria, An overview of ABRACOS, in *Amazon Deforestation and Climate*, edited by Gash et al., 1–14, John Wiley, New York, 1996.
- Greco, S., R. Swap, M. Garstang, S. Ulanski, M. Shipham, R. C. Harriss, R. Talbott, M. O. Andreae, and P. Artaxo, Rainfall and surface kinematic conditions over central Amazonia ABLE 2B, *J. Geophys. Res.*, *95*, 17,001–17,014, 1990.
- Greco, S., J. Scala, J. Halverson, H. L. Massie Jr., W. K. Tao, and M. Garstang, Amazon coastal squall lines, Part II, Heat and moisture transports, *Mon. Weather Rev.*, *122*, 623–635, 1994.
- LeMone, M. A., E. J. Zipser, and S. B. Trier, The role of environmental shear and thermodynamic conditions in determining the structure and evolution of mesoscale convective systems during TOGA COARE, *J. Atmos. Sci.*, *55*(23), 3493–3518, 1998.
- Machado, L. A. T., H. Laurent, and A. Lima, The diurnal march of the convection observed during TRMM-WETAMC/LBA, *J. Geophys. Res.*, *107*, 10.1029/2001JD000338, in press, 2002.
- Nobre, C. A., P. J. Sellers, and J. Shukla, Amazonian deforestation and regional climate change, *J. Clim.*, *4*, 957–987, 1991.
- Pereira Filho, A. J., M. A. F. Silva Dias, R. I. Albrecht, L. G. P. Preira, and O. Massambani, Multisensor analysis of a squall line in the Amazon region, *J. Geophys. Res.*, *107*, 10.1029/2001JD000305, in press, 2002.
- Petersen, W. A., L. D. Carey, S. A. Rutledge, J. C. Knievel, N. J. Doesken, R. H. Johnson, T. B. McKee, T. Vonder Haar, and J. F. Weaver, Mesoscale and radar observations of the Fort Collins flash flood of 28 July 1997, *Bull. Am. Meteorol. Soc.*, *80*, 191–216, 1999.
- Pielke, R. A., W. R. Cotton, R. L. Walko, C. J. Tremback, W. A. Lyons, L. D. Grasso, M. E. Nicholls, M. D. Moran, D. A. Wesley, T. J. Lee, and J. H. Copeland, A comprehensive meteorological modeling system - RAMS, *Meteorol. Atmos. Phys.*, *49*(1–4), 69–91, 1992.
- Silva Dias, M. A. F., and R. N. Ferreira, Application of a linear spectral model to the study of Amazonian squall lines during GTE/ABLE 2B, *J. Geophys. Res.*, *97*, 20,405–20,419, 1992.
- Silva Dias, M. A. F., and P. Regnier, Simulation of mesoscale circulations in a deforested area of Rondonia in the dry season, in *Amazonian Deforestation and Climate*, edited by J. Gash et al., pp. 531–547, John Wiley, New York, 1996.
- Silva Dias, M. A. F., et al., Clouds and rain processes in a biosphere atmosphere interaction context in the Amazon Region, *J. Geophys. Res.*, *107*, 10.1029/2001JD000335, in press, 2002.
- Souza, E. P., N. O. Rennó, and M. A. F. Silva Dias, Convective circulations induced by surface heterogeneities, *J. Atmos. Sci.*, *57*, 2915–2922, 2001.
- Takahashi, T., Near absence of lightning in torrential rainfall producing Micronesian thunderstorms, *Geophys. Res. Lett.*, *17*, 2381–2384, 1990.
- Tompkins, A. M., Organization of tropical convection in low vertical wind shears: The role of cold pools, *J. Atmos. Sci.*, *58*, 1650–1672, 2001.
- Trier, S. B., W. C. Skamarock, M. A. LeMone, D. B. Parsons, and D. P. Jorgensen, Structure and evolution of the 22 February 1993 TOGA COARE squall line: Numerical simulations, *J. Atmos. Sci.*, *53*, 2861–2886, 1996.
- Walko, R. L., W. R. Cotton, M. P. Meyers, and J. Y. Harrington, New RAMS cloud microphysics parameterization, Part I, The single-moment scheme, *Atmos. Res.*, *38*, 29–62, 1995.
- Wang, J. R. L. Bras, and E. A. B. Eltahir, The impact of observed deforestation on the mesoscale distribution of rainfall and clouds in Amazonia, *J. Hydrometeorol.*, *1*, 267–286, 2000.

R. I. Albrecht, M. Longo, M. A. F. Silva Dias, and P. L. Silva Dias, Department of Atmospheric Science, University of São Paulo (USP), Rua do Matão, 1226, 05508-900 São Paulo - SP, Brazil. (mafdsdia@model.iag.usp.br)

R. Cifelli and W. Petersen, Department of Atmospheric Science, Colorado State University (CSU), Fort Collins, CO 80523 USA.

A. K. Betts, Atmospheric Research, Pittsford, VT, USA.

M. A. Antonio, A. M. Gomes, and M. A. Lima, Institute of Meteorological Research, State University of São Paulo (UNESP), Brazil.

G. F. Fisch, Institute of Space Activities, Aeronautics Technological Center (CTA), USA.